

1 Biomass burning impact on CCN number, hygroscopicity and cloud 2 formation during summertime in the eastern Mediterranean

3 A. Bougiatioti^{1,2,3}, S. Bezantakos^{4,5}, I. Stavroulas³, N. Kalivitis³, P. Kokkalis^{2,11}, G.
4 Biskos^{6,7}, N. Mihalopoulos^{3,7,10}, A. Papayannis², A. Nenes^{1,8,9,10}

5
6 ¹School of Earth and Atmospheric Sciences, Georgia Institute of Technology, Atlanta, GA, USA

7 ²Laser Remote Sensing Unit, National Technical University of Athens, Zografou, Athens, Greece

8 ³ECPL, Department of Chemistry, University of Crete, Voutes, 71003 Heraklion, Greece

9 ⁴Department of Environment, University of the Aegean, Mytilene, 81100, Greece

10 ⁵Institute of Nuclear Technology and Radiation Protection, NCSR "Demokritos", 15310 Ag. Paraskevi,
11 Athens, Greece

12 ⁶Faculty of Civil Engineering and Geosciences, Delft University of Technology, Delft 2728 CN, The
13 Netherlands

14 ⁷Energy Environment and Water Research Center, The Cyprus Institute, Nicosia 2121, Cyprus

15 ⁸School of Chemical & Biomolecular Engineering, Georgia Institute of Technology, Atlanta, GA, USA

16 ⁹Institute of Chemical Engineering Sciences (ICE-HT), FORTH, Patras, Greece

17 ¹⁰IERSD, National Observatory of Athens, P. Penteli 15236, Athens, Greece

18 ¹¹IAASARS, National Observatory of Athens, P. Penteli 15236, Athens, Greece

19 20 **Abstract**

21 This study investigates the concentration, cloud condensation nuclei (CCN) activity and
22 hygroscopic properties of particles influenced by biomass burning in the eastern
23 Mediterranean and their impacts on cloud droplet formation. Air masses sampled were
24 subject to a range of atmospheric processing (several hours up to 3 days). Values of
25 the hygroscopicity parameter, κ , were derived from CCN measurements and a
26 Hygroscopic Tandem Differential Mobility Analyzer (HTDMA). An Aerosol Chemical
27 Speciation Monitor (ACSM) was also used to determine the chemical composition and
28 mass concentration of non-refractory components of the submicron aerosol fraction.
29 During fire events, the increased organic content (and lower inorganic fraction) of the
30 aerosol decreases the values of κ , for all particle sizes. Particle sizes smaller than 80
31 nm exhibited considerable chemical dispersion (where hygroscopicity varied up to
32 100% for particles of same size); larger particles, however, exhibited considerably less
33 dispersion owing to the effects of condensational growth and cloud processing. ACSM
34 measurements indicate that the bulk composition reflects the hygroscopicity and
35 chemical nature of the largest particles (having a diameter of ~100 nm at dry
36 conditions) sampled. Based on Positive Matrix Factorization (PMF) analysis of the
37 organic ACSM spectra, CCN concentrations follow a similar trend as the biomass
38 burning organic aerosol (BBOA) component, with the former being enhanced between
39 65 and 150% (for supersaturations ranging between 0.2 and 0.7%) with the arrival of
40 the smoke plumes. Using multilinear regression of the PMF factors (BBOA, OOA-BB
41 and OOA) and the observed hygroscopicity parameter, the inferred hygroscopicity of
42 the oxygenated organic aerosol components is determined. We find that the
43 transformation of freshly-emitted biomass burning (BBOA) to more oxidized organic
44 aerosol (OOA-BB) can result in a twofold increase of the inferred organic
45 hygroscopicity; about 10% of the total aerosol hygroscopicity is related to the two
46 biomass burning components (BBOA and OOA-BB), which in turn contribute almost

47 35% to the fine-particle organic water of the aerosol. Observation-derived calculations
48 of the cloud droplet concentrations that develop for typical boundary layer clouds
49 conditions suggest that biomass burning increases droplet number, on average by
50 8.5%. The strongly sublinear response of clouds to biomass burning (BB) influences is
51 a result of strong competition of CCN for water vapor, which results in very low
52 maximum supersaturation (0.08% on average). Attributing droplet number variations
53 to the total aerosol number and the chemical composition variations shows that the
54 importance of chemical composition increases with distance, contributing up to 25%
55 of the total droplet variability. Therefore, although BB burning may strongly elevate
56 CCN numbers, the impact on droplet number is limited by water vapor availability and
57 depends on the aerosol particle concentration levels associated with the background.

58
59

60 **1. Introduction**

61 Globally, biomass burning (BB) is a major source of atmospheric aerosols (Andreae et
62 al., 2004). In the eastern Mediterranean, up to one third of the dry submicron aerosol
63 mass during the summer period consists of highly oxidized organic compounds
64 (Hildebrandt et al., 2010). During July-September, biomass-burning aerosol originates
65 from long-range transport from southern Europe and countries surrounding the Black
66 Sea (Sciare et al., 2008). Bougiatioti et al. (2014) showed that of the total organic
67 aerosol (OA), about 20% is freshly-emitted biomass burning organic aerosol (BBOA),
68 30% is oxidized, processed OA originating from BBOA (BB-OOA), and the remaining
69 50% is highly oxidized aerosol that results from extensive atmospheric aging. Hence,
70 in terms of organic mass, during time periods of high biomass burning activity, at least
71 50% of the aerosol can be attributed to BB emissions.

72 Aerosol liquid water content (LWC) is a key medium for atmospheric chemistry that
73 also drives the partitioning of soluble organic vapors to the particle phase (Carlton and
74 Turpin, 2013). LWC is a prime modulator of aerosol direct radiative forcing (e.g., Pilinis
75 et al., 1995), and by promoting secondary aerosol formation it can influence aerosol
76 mass and number that impact both the aerosol direct and indirect effect (Kanakidou
77 et al., 2005).

78 Biomass burning aerosol particles have the potential to act as cloud condensation
79 nuclei (CCN), thereby impacting on cloud properties and climate. Modeling studies
80 suggest that BB is a significant global source of CCN number (Spracklen et al., 2011).
81 Laboratory and field studies have shown that biomass burning aerosol is highly
82 hygroscopic and water-soluble, exhibiting up to about half the water uptake capacity
83 of ammonium sulfate (Asa-Awuku et al., 2008; Cerully et al., 2014). Engelhart et al.
84 (2012) found that freshly emitted BBOA displays a broad range of hygroscopicity (κ
85 parameter from 0.06 to 0.6) that considerably reduces after just a few hours of
86 photochemical aging, to a κ value of 0.2 ± 0.1 (Petters and Kreidenweis, 2007). Few
87 studies, however, focus on the hygroscopicity of ambient BB aerosol as a function of
88 atmospheric age extending out to a few days. Relatively few studies also go beyond
89 CCN to calculations of droplet number (e.g., Roberts et al., 2003), and even fewer
90 studies characterize the relative role of aerosol number and chemical composition
91 (hygroscopicity) variability to the predicted droplet number variability in clouds formed

92 from BB-influenced air masses. These issues are important, because the
93 supersaturation that develops in clouds is not known beforehand, nor constant, but
94 rather a strong function of the CCN levels and cloud dynamical forcing (updraft
95 velocity).

96 In the current study we focus on the hygroscopicity, CCN concentrations and resulting
97 droplet formation characteristics (droplet number and cloud supersaturation)
98 associated with air masses influenced by summertime biomass burning events in the
99 eastern Mediterranean. The smoke-laden air masses sampled were subject to a range
100 of atmospheric processing (several hours up to 3 days), identified using remote
101 sensing techniques (Moderate Resolution Imaging Spectroradiometer, Kaufman and
102 Remer, 1994; Cloud-Aerosol Lidar with Orthogonal Polarization, Winker et al., 2009,
103 Mamouri et al., 2012), backtrajectory analysis and other in-situ chemical metrics.
104 Values of the hygroscopicity parameter, κ , were derived from CCN and HTDMA
105 measurements and linked to distinct chemical constituents identified with Positive
106 Matrix Factorization of the chemical constituents measured with an Aerosol Chemical
107 Speciation Monitor (ACSM). Finally, the observations are used to predict the cloud
108 droplet number and supersaturation formed in clouds that develop in each air mass,
109 focusing on the contribution of aerosol number and hygroscopicity to the predicted
110 droplet number variability. This is one of the very few field studies that use in-situ
111 observations to i) unravel the contributions of composition and aerosol size to BB-
112 related CCN distributions and their impacts on cloud droplet number, ii) quantify the
113 contributions of biomass burning constituents to aerosol hygroscopicity and liquid
114 water in the region.

115

116 **2. Experimental Methods**

117 *2.1 Sampling site and period*

118 The measurements were performed at the Finokalia atmospheric background station
119 (35°32'N, 25°67'E; <http://finokalia.chemistry.uoc.gr>) of the University of Crete, which
120 is part of the Aerosols, Clouds, and Trace gases Research Infrastructure Network
121 (ACTRIS; <http://www.actris.net/>). More details about the sampling site are provided
122 by Mihalopoulos et al. (1997) and Sciare et al. (2003). Although measurements took
123 place from mid-August to mid-November 2012, the focus of our analysis involves the
124 periods of intense biomass burning influence, August to September 2012. BB plumes
125 sampled were fresh, originating from the Greek islands and mainland (transport time
126 6-7 h) but also from long-range transport from the Balkans (transport time > 1 day)
127 as determined by using HYSPLIT backtrajectory analysis as shown in detail in
128 Bougiatioti et al. (2014) combined with the hot spots/fire data from MODIS/Fire
129 Information for Resource Management System (FIRMS; Remy and Kaiser, 2014).

130 *2.2 Instrumentation and methodology*

131 Chemical composition and mass concentration of non-refractory components
132 (ammonium, sulfate, nitrate, chloride and organics) of the submicron aerosol fraction
133 was provided by an Aerodyne Research Aerosol Chemical Speciation Monitor (ACSM;
134 Ng et al., 2011) with a temporal resolution of 30 minutes. More details of the ACSM

135 measurements and subsequent analysis can be found in Bougiatioti et al. (2014). Total
136 absorption measurements provided the black carbon (BC) concentrations by a seven-
137 wavelength aethalometer (Magee Scientific, AE31). From the BC measurements and
138 using the approach of Sandradewi et al. (2008) the wood-burning and fossil fuel
139 contribution to the total BC concentrations were calculated, using an absorption
140 exponent of 1.1 for fossil fuel burning and 1.86 for pure wood burning. The aerosol
141 particle size distributions from 9 to 850 nm were measured with a 5-min resolution by
142 a custom-built scanning mobility particle sizer (SMPS; TROPOS-type, Wiedensohler et
143 al., 2012) equipped with a condensation particle counter (CPC; TSI model 3772;
144 Stolzenburg and McMurry, 1991). Sample humidity was regulated below the relative
145 humidity of 40% with the use of Nafion[®] dryers in both aerosol and sheath flow and
146 the measured number size distributions were corrected for diffusional particle losses
147 (Kalivitis et al. 2015).

148 A Continuous Flow Stream-wise Thermal Gradient CCN Chamber (CFSTGC; Roberts
149 and Nenes, 2005) was used in parallel with a Hygroscopic Tandem Differential Mobility
150 Analyzer (HTDMA; Rader and McMurry, 1986) to measure the CCN number, activity
151 and hygroscopicity of ambient aerosol for supersaturated (0.1-0.7%) and subsaturated
152 conditions (relative humidity, RH=86%), respectively. The whole system, which is
153 illustrated in Figure 1, sampled air with a total flow-rate of 1.8 L min⁻¹. After passing
154 through a Nafion dryer (MD-110-12S-2, Perma Pure LLC, RH<30%) the dried particles
155 were selected based on their electrical mobility by a Differential Mobility Analyzer
156 (DMA-1; TSI Model 3080; Knutson and Whitby, 1975). The sheath flow and classified
157 aerosol outlet flow of DMA-1 were 10.8 and 1.8 L min⁻¹, respectively, while the mobility
158 diameter was changed every 6 minutes between 60, 80, 100 and 120 nm.

159 The classified aerosol from DMA-1 was then split into two streams. The first stream
160 was passed through a Nafion-tube humidity exchanger where its RH was increased to
161 86%. The size distribution of the RH-conditioned particles was determined by a second
162 DMA (DMA-2; custom-made DMA using a closed-loop sheath flow with RH control;
163 Biskos et al., 2006; Bezantakos et al., 2013) coupled with a Condensation Particle
164 Counter (CPC, TSI Model 3772). The RH in both the aerosol and the sheath flow in
165 DMA-2 was controlled by PID controllers to within $\pm 2\%$ accuracy. Both DMAs in the
166 HTDMA system were calibrated with Polystyrene Latex (PSL) spheres. The other
167 classified stream was introduced into the CFSTGC to measure the CCN activity of
168 particles. The CFSTGC was operated in Scanning Flow CCN Analysis (SFCA) mode
169 (Moore and Nenes, 2009), in which the flow rate in the growth chamber changes over
170 time, while a constant streamwise temperature difference is applied. This causes
171 supersaturation to change continuously, allowing the rapid and continuous
172 measurement of CCN spectra with high temporal resolution. The SFCA cycle used
173 involved first increasing the flow rate linearly between a minimum flow rate ($Q_{min} \sim$
174 $300 \text{ cm}^3 \text{ min}^{-1}$) and a maximum flow rate ($Q_{max} \sim 1000 \text{ cm}^3 \text{ min}^{-1}$) over a ramp time
175 of 60 seconds. The flow was maintained at Q_{max} for 10 seconds and then linearly
176 decreased to Q_{min} over 60 s. Finally, the flow rate was held constant at Q_{min} for 10 s
177 and the scan cycle was repeated. The activated droplets in the CFSTGC were counted
178 and sized at the exit of its growth chamber with an Optical Particle Counter (OPC) that

179 detects droplets and classifies them into 20 size bins with diameter ranging from 0.7
180 to 10 μm every 1 s.

181 The water vapor supersaturations developed in the CFSTGC during an SFCA cycle were
182 characterized with ammonium sulfate calibration aerosol following the procedure of
183 Moore and Nenes (2009). In brief, an ammonium sulfate solution was atomized, dried,
184 charge-neutralized and classified by DMA-1. The resulting monodisperse aerosol flow
185 was split between DMA-2 and the CFSTGC, operating in SFCA mode and with a CFSTGC
186 streamwise temperature difference of $\Delta T=5$ K. From this setup, we obtain the
187 instantaneous concentrations of the classified aerosol and the resulting CCN during
188 the SFCA flow cycles. . The ratio of CCN to total aerosol number gives the activation
189 ratio, R_a , which varies with the instantaneous volumetric flow rate, Q , in the CFSTGC.
190 Using data from multiple SFCA flow cycles, R_a is then fit to a sigmoid function that
191 depends on Q :

$$192 \quad R_a \equiv \frac{CCN}{CN} = a_0 + \frac{a_1 - a_0}{1 + (Q/Q_{50})^{-a_2}} \quad (1)$$

193 where a_0 , a_1 , a_2 and Q_{50} , are constants which describe the minimum, maximum, slope
194 and inflection point of the sigmoidal, respectively. The "critical flow rate", Q_{50} ,
195 corresponds to the instantaneous flow rate that produces a level of supersaturation,
196 s , required to activate the measured monodisperse aerosol. s is determined from the
197 size of the classified aerosol using Köhler theory (Moore et al., 2012a).

198 .
199 Repeating the procedure for many sizes of classified ammonium sulfate results in the
200 SFCA calibration curve, which gives the supersaturation in the CFSTGC as a function
201 of flow rate (i.e Q_{50} vs. s) throughout an SFCA flow cycle. Absolute uncertainty of the
202 calibrated CCNC supersaturation is estimated to be $\pm 0.04\%$ (Moore et al., 2012a;
203 2012b).

204 In our instrument setup, R_a can change either from variations in the size of the
205 monodisperse aerosol, d_p , or the instrument supersaturation, s (or flow rate, Q). The
206 independently varied parameter is indicated hereon in parentheses in front of the
207 activation ratio, e.g., $R_a(Q)$, $R_a(s)$, $R_a(d_p)$ for R_a as a function of Q , s and d_p ,
208 respectively.

209 Analysis of R_a obtained for our experimental setup for ambient particles samples
210 provide very important information on the activity and chemical mixing state of the
211 CCN. This is carried out as follows. For every particle size d_p set by the DMA-1, $R_a(Q)$,
212 is measured at every instant in the CFSTGC according to Eq.1. Typically $a_0 \ll a_1$;
213 given that Q and s are related through the calibration, $R_a(Q)$ data can be transformed
214 to $R_a(s)$ as:

$$215 \quad R_a(s) = \frac{E}{1 + \left(\frac{s}{s^*}\right)^C} \quad (2)$$

216 where s , s^* correspond to Q , Q_{50} of the monodisperse aerosol. E and C are parameters
217 determined from fitting. According to Cerully et al. (2011), $R_a(s)$ represents a
218 cumulative distribution of critical supersaturation for particles with dry diameter d_p ;

219 Köhler theory can then be applied to express $R_a(s)$ in terms of the hygroscopicity
 220 parameter $R_a(\kappa)$:

$$221 \quad R_a(\kappa) = \frac{E}{1 + \left(\frac{\kappa}{\kappa^*}\right)^{C/2}} \quad (3)$$

222 where $\kappa = \frac{4A^3}{27d_p^3s^2}$ expresses the dependence of κ on d_p and s , $A = \frac{4M_w\sigma_w}{RT\rho_w}$ is the

223 Kelvin parameter, whereas M_w , σ_w and ρ_w are respectively the molar mass, the surface
 224 tension and the density of water, R is the universal gas constant, and T is temperature.

225 In equations 2, 3, s^* and κ^* correspond to the characteristic critical supersaturation
 226 and hygroscopicity parameter of the monodisperse aerosol, respectively, and
 227 correspond to the most probable value of the parameters (Cerully et al., 2011). From
 228 Equation 3, the probability distribution function for κ , $p^s(\kappa)$, can be derived for the
 229 ambient monodisperse aerosol (Cerully et al., 2011):

$$230 \quad p^s(\kappa) = \frac{1}{E} \frac{dR_a(\kappa)}{d\kappa} = -\frac{\frac{C}{\kappa^* 2} \left(\frac{\kappa}{\kappa^*}\right)^{\frac{C}{2}-1}}{\left(1 + \left(\frac{\kappa}{\kappa^*}\right)^{\frac{C}{2}}\right)^2} \quad (4)$$

231 Analysis of $p^s(\kappa)$ can provide a direct measure of the chemical heterogeneity of the CCN
 232 population. For this, we adopt the metric of chemical dispersion, $\sigma(\kappa)$, introduced by
 233 Lance (2007) and further developed in Cerully et al. (2011) and Lance et al. (2013):

$$234 \quad \sigma^2(\kappa) = \frac{\int_0^1 (\kappa - \kappa^*)^2 p^s(\kappa) d\kappa}{\int_0^1 p^s(\kappa) d\kappa} \quad (5)$$

235 $\sigma(\kappa)$ is the square root of variance of κ^* ; as the chemical heterogeneity of the CCN
 236 increases, the distribution of κ broadens, and $\sigma(\kappa)$ becomes larger so that the range in
 237 CCN hygroscopicity is given by $\kappa^* \pm \sigma(\kappa)$.

238 Particle water uptake at sub-saturated conditions in the Nafion-tube humidity
 239 exchanger and DMA-2 was also evaluated by the growth factor measured for the
 240 calibration $(\text{NH}_4)_2\text{SO}_4$. Particle hygroscopic growth at sub-saturated conditions (g_i) is
 241 obtained by:

$$242 \quad g(RH) = \frac{d_m(RH)}{d_p} \quad (6)$$

243 where $d_m(RH)$ and d_p are the geometric mean mobility diameters of the sampled
 244 particles at the hydrated state (i.e. at RH=86%) as measured by DMA-2 and the CPC,
 245 and at the dry state selected by DMA-1 (RH < 30%), respectively. Particle size
 246 distributions at 86% RH were inverted using the TDMAfit algorithm (Stolzenburg and
 247 McMurry, 1988) which is also capable of distinguishing between internally and
 248 externally mixed aerosols (e.g. Bezantakos et al., 2013).

249 Hygroscopicities determined from the CCN measurements are differentiated by
 250 corresponding values from the HTDMA measurements by adding a subscript CCN, or
 251 HTDMA, respectively (e.g. κ_{HTDMA} , κ_{CCN}). κ_{HTDMA} is calculated from the HTDMA-
 252 measured sub-saturated hygroscopic growth factors using:

$$253 \quad \kappa_{HTDMA} = (g(RH))^3 - 1 \left(\frac{\exp\left(\frac{A}{g(RH) * d_p}\right) - 1}{\frac{RH}{100\%}} \right) \quad (7)$$

254 with A being the Kelvin parameter defined in Equation 3. The exponential term of this
 255 equation (i.e. the Kelvin term) is used to account for curvature effects on vapor
 256 pressure.

257 An average value of the hygroscopic parameter at each dry particle size, d_p , which is
 258 representative of the hygroscopic properties of the entire particle population is
 259 obtained as follows:

$$260 \quad \overline{\kappa_{HTDMA}} = \int_{g_{min}}^{g_{max}} \kappa(g_{(RH)}) p(g_{(RH)}) dg_{(RH)} \quad (6)$$

261 where $\kappa(g_{(RH)})$ is obtained from the growth factor probability distribution using
 262 equation 5 and $p(g_{(RH)})$ is the probability of each growth factor. g_{min} , g_{max} are the
 263 minimum and maximum growth factors, respectively, obtained from the growth factor
 264 probability distribution and represent the minimum and maximum g with non-zero
 265 probability value.

266 To support the *in situ* instruments, we used space-borne laser remote sensing (lidar)
 267 data from CALIOP (Mamouri et al., 2009; Winker et al., 2009) to characterize the
 268 plumes emerging from the fire hot spots. The fire plume originating from any location
 269 can be tracked by HYSPLIT back-trajectory analysis (Bougiatioti et al., 2014) and lidar
 270 observations can be used to check the presence of aerosol layers and aerosol types.
 271 Optical confirmation of the smoke plumes is provided by MODIS and FIRMS as shown
 272 in the supplementary material of Bougiatioti et al. 2014.

273

274 **3. Results and Discussion**

275 **3.1 Identifying periods of biomass burning influence**

276 Bougiatioti et al. (2014) identified the BB events analyzed here by the time evolution
 277 of absorption enhancements (BC) in the aerosol, which was further verified by FIRMS
 278 and back-trajectory analysis. During these events mass spectrometric biomass burning
 279 tracers (i.e. fragments $m/z=60$ and 73) also exhibited elevated levels. Clear biomass
 280 burning contribution was identified by source apportionment using Positive Matrix
 281 Factorization (PMF) analysis for four distinct events. The BB events considered include
 282 a severe fire event that burned most of the island of Chios (19–21 August), an
 283 extensive wildfire at the Dalmatian Coast in Croatia resulting in smoke plumes that
 284 spread across the Balkans during the period 28–30 August, and, less extensive fires
 285 on the Greek islands of Euboea (3-5 September) and Andros (12-13 September). All
 286 fire events exhibited discrete BBOA profiles depending on the biomass burning fuel, as
 287 presented in detail by Bougiatioti et al. (2014). Nevertheless, the organic aerosol

288 derived from the aging of the biomass burning aerosol (OOA-BB) identified for all
289 events had a similar profile, regardless of the BBOA it was derived from (Bougiatioti et
290 al. 2014). Transport time estimate and backtrajectory analysis were conducted with
291 the Plume Arrival (h) from Base Time graphics with the help of the HYSPLIT model
292 (www.arl.noaa.gov/hysplit.php).

293 MODIS and CALIOP measurements confirm the validity of the Bougiatioti et al. (2014)
294 analysis, by clearly showing the origin, transport path and characteristics of the
295 biomass burning plume from the Chios fire on 18 and 19 August 2012, respectively.
296 Indeed, in Figure 2a we show the MODIS true color image showing the plume
297 emerging from the Chios fires on 18 August 2012 as obtained during its 9.39 UTC
298 overpass over Greece (Kyzirakos et al., 2014). The blue and red lines delineate the
299 ground track of the CALIPSO satellite during its overpass over Crete several hours later
300 on 19 August 2012 (the first between 00:27-00:40 and the second between 11:34-
301 11:47 UTC); the red star shows the sampling site at Finokalia station. The CALIPSO
302 vertical profiles of the aerosol backscatter coefficient (in $\text{km}^{-1}\text{sr}^{-1}$) at 532 and 1064 nm
303 for the two overpasses are shown in Figure 2b (left-hand side) together with the
304 corresponding linear particle depolarization ratio at 532 nm obtained between
305 00:27:30-00:40 UTC (right-hand side). Comparing the midnight and the daytime
306 aerosol backscatter profiles in Figure 2b, we observe that the midnight values are 3-4
307 times lower than the daytime ones for altitudes up to 3 km height. In addition, the
308 daytime observations show a discrete aerosol layer below 1.5 km. As for the linear
309 particle depolarization ratio it shows a mean value of 19% up to 1.25 km height and
310 less than 6-10% above (1.25-2 km).

311 Finally, we made use of the classification scheme of the CALIPSO data (Omar et al.,
312 2009) to classify the different subtypes of aerosols in the plume captured during its
313 first overpass over Crete on 19 August 2012 (00:27-00:40 UTC). This classification
314 scheme, based on the optical and microphysical properties of the sampled aerosols
315 indeed reveals the presence of a mixture of smoke, polluted dust and marine particles
316 observed below a 3 km altitude (black color for smoke, brown for polluted dust and
317 blue for marine) as shown in Figure 2c, within the depicted area between 39°N, 24.1°E-
318 37°N, 23.4°E, just NW of the Finokalia station and along the CALIPSO ground track.
319 According to this classification, over Crete the presence of polluted dust (mixed with
320 smoke and marine aerosols) prevails within the marine boundary layer, which for
321 Finokalia is approximately 1 km (Kalivitis et al., 2007), extending up to 0.8-1.2km
322 height. This implies that for the 00:27–00:40 UTC time slot, the BB aerosols sampled
323 by the ground-based in situ measurements at Finokalia would contribute less (due to
324 dilution) to the global aerosol mass loading than, if measured, over the western Crete.

325
326

3.2 PM₁ composition

327 The average mass concentration for the whole measurement period (mid-August to
328 mid-November 2012), based on the ACSM measurements combined with BC from the
329 aethalometer was $9.2 \pm 4.8 \mu\text{g m}^{-3}$. The corresponding median concentrations for the
330 main aerosol constituents were 3.56, 1.31, 3.03 and $0.47 \mu\text{g m}^{-3}$ for sulfate,
331 ammonium, organics and BC respectively. Figure 3 represents the time series of the
332 major submicron species where it can be seen that during the fire events the

333 contribution of organics and BC increased substantially (from 34.9 to 46.5% for
334 organics and from 6.1 to 9.5% for BC) with a simultaneous reduction of that of sulfate.
335 Source apportionment clearly shows that these increases are related to BB influences
336 (Bougiatioti et al. 2014). During all BB events there is a clear dominance of wood
337 burning over fossil fuel contributions to BC. The wood burning component of BC is also
338 provided as a reference, depicting the enhanced contribution of biomass burning
339 during the highlighted events.

340 Based on the size-resolved CCN activity measurements and the inferred hygroscopicity
341 parameter κ of the aerosol (Equation 3), it is evident that the changes in the organics
342 and sulfate mass fractions will also influence the CCN concentrations, activation
343 fractions and hygroscopicity. As the ACSM provides bulk submicron chemical
344 composition and thus, is not able to capture any sized-dependent chemical
345 composition, the size-resolved CCN activity measurements are able to resolve distinct
346 CCN activity and mixing state of the different particle sizes. These aspects are
347 thoroughly investigated in the following sections.

348

349 ***3.3 CN and CCN number concentrations and biomass burning events***

350 For all four events of biomass burning-influenced air masses arriving at Finokalia, the
351 observed aerosol number concentration increased considerably, regardless of size. The
352 increases are quantitatively expressed using averaged data from at least 6 hours prior
353 to the arrival time of the BB smoke. For particle sizes above 100 nm, BB increased
354 concentrations by 65% for the Chios fire, around 50% for the Croatia fire, 88% for
355 the Euboea fire and about 150% for the Andros fire. Less pronounced increases were
356 seen for the smaller particle sizes. The corresponding impacts on CCN
357 concentrations for the classified aerosol are shown in Figure 4 for all fire events.
358 Concentrations are given at the characteristic supersaturation, s^* , of the monodisperse
359 CCN as classified by DMA-1 (Section 2.2). Within each event, s^* did not vary by more
360 than 13.6%; therefore most of the variability in CCN number can be attributed to
361 variations in the size distribution, rather than shifts in the chemical composition (i.e.,
362 s^*).

363 As expected, smaller particles exhibit a higher critical supersaturation (Bougiatioti et
364 al., 2011). During periods with smoke influence, critical supersaturations tend to
365 increase, indicating that particles associated with BB are less effective CCN compared
366 to those of the background aerosol. To quantify the direct influence of biomass burning
367 to particle and CCN number concentrations we studied the concentration of the BBOA
368 component, identified by PMF analysis of the ACSM mass spectra (Bougiatioti et al.,
369 2014). The BBOA concentration time series depicts the arrival time of the smoke and
370 the intensity of the BB influence.

371 The data shown in Figure 4 indicates that during the majority of the identified biomass
372 burning events, CCN concentrations for the larger particle sizes increase, and follow
373 the BBOA trend. This increase was more pronounced, depending on the proximity of
374 the fire and therefore, the travel time of the air masses. Rose et al. (2010) also
375 observed increases in CCN during a biomass burning event near the mega-city
376 Guangzhou, China, where CCN number concentrations at $s=0.068\%$ and 0.27% ,

377 increased by 90% and 8%, respectively. The same study attributed these changes to
378 increases in the particle size when BB influence was present.

379 Of all particle sizes examined, it appears that those having mobility diameter of 60 nm
380 exhibit the least variability in terms of CCN number concentration before and during
381 the BB influence (Figure 4, open circles). The concentration, however, significantly
382 increase during the BB event from Croatia (Figure 4b). This event, together with others
383 of smaller extent, is associated with new particle formation (NPF) events. The observed
384 frequency of NPF days at Finokalia is close to 30% (Kalivitis et al., 2015), regardless
385 of the presence or not of BB-laden air masses. Based on aerosol chemical composition,
386 it appears that both gaseous sulfuric acid and organic compounds take part in the
387 growth of nucleated particles to CCN-relevant sizes. These organic compounds that
388 contribute to the nuclei growth may be of different origins including biogenic
389 emissions, biomass burning and other possible anthropogenic sources from long-range
390 transport (Kalivitis et al. 2015). From Figure 4b it appears that when the BB event is
391 combined with such a NPF event within a few hours, 60-nm particles are strongly
392 influenced and their CCN concentrations increase considerably. The influence of BB to
393 the hygroscopicity of 60-nm particles and the other sizes is examined in a subsequent
394 section. A detailed discussion on these events and their contribution to CCN
395 concentrations is provided by Kalivitis et al. (2015).

396

397

3.4 CCN activation fractions during fire events

398 As demonstrated in the preceding section, CCN number concentrations during the
399 biomass burning events proportionately increased for the larger particle sizes. Figure
400 5 shows the activation fractions ($R_a(Q)$) for three of the four particle sizes and the four
401 considered fire events (120 nm is not shown as it exhibits the same behavior as 100
402 nm). As an indicator of BB influence, we use the concentration of the aged BB factor
403 identified in the ACSM spectra (OOA-BB), as it represents the atmospherically-
404 processed component of BBOA. This factor is chosen as it constitutes a larger part of
405 the organic aerosol (30%) with BB influence and whose ageing is expected to be
406 reflected in terms of CCN activity.

407 For all particle sizes, the activation fractions are derived from the asymptote of the
408 fitting to the sigmoidal function of the $R_a(s)$ during each supersaturation cycle and
409 represents the CCN behavior at the highest supersaturations measured ($s > 0.6\%$).
410 Figure 5 shows that even though CCN concentrations increase for particles larger than
411 80 nm, their activation fractions remain, more or less, stable and very close to unity
412 throughout the events. This observation implies that almost all aerosol particles larger
413 than 80 nm are CCN active at supersaturations higher than 0.6%, within uncertainties.
414 This is not the case for 60 nm particles whose activation fractions at 0.6% s (and in
415 the case of the Chios fire activation fractions of 80 nm particles as well at 0.4% s)
416 exhibit the highest variability, with ratios approaching values as low as 40%. It can be
417 seen that as concentrations of the OOA-BB start to increase, the activation fractions
418 of 60 nm particles at $\sim 0.6\%$ s start to diminish. It thus appears that larger particles
419 are mostly internally mixed, as also seen by their high activation ratios, while small
420 particles could be externally mixed populations. An indication of the heterogeneity of
421 the smaller particle sizes compared to the larger ones is the slope of the sigmoid fit to

422 the $Ra(s)$; the steeper the slope, the more homogeneous the population, and given
423 that the 60 nm particles exhibited the broader slopes, the more heterogeneous these
424 particles are. This can be explained by a size-dependent chemical composition and the
425 presence of a population with notable lower hygroscopicity that prohibits the particles
426 from acting as CCN and can be attributed to different sources and atmospheric
427 processing (coagulation, cloud processing and condensation of secondary aerosol) that
428 generally tend to internally mix the particles, rendering them more CCN active. Indeed,
429 the lowest activation fractions occur for the strongest events where the time for
430 transport and aging is most limited (hence least aged and hygroscopic). The particle
431 chemical dispersion retrievals (Section 3.5) also supports this view. The same
432 conclusion is also drawn from the data provided by Bougiatioti et al. (2011) for the
433 same sampling site during summertime, and are verified by analysis of the chemical
434 dispersion and HTDMA data shown in following sections. The evolution of the mixing
435 state of each particle size is further investigated by the HTDMA measurements in a
436 subsequent section (Section 3.6) as well.

437

438 ***3.5 Hygroscopicity and chemical heterogeneity during the biomass*** 439 ***burning events***

440 The characteristic hygroscopicity parameters, κ^* , derived from the CCN measurements
441 for all particle sizes and for the four selected fire events are presented in Figure 6. As
442 a reference for the arrival time and magnitude of the event, the concentration of the
443 BBOA factor is also shown in the figure, which has the characteristics of the freshly-
444 emitted BB aerosol and is expected to influence more the hygroscopicity of the
445 particles. The smaller particles have the lowest κ_{CCN} values, and hygroscopicity
446 consistently increased with size. This hygroscopicity trend has also been observed
447 elsewhere (Dusek et al., 2010; Cerully et al., 2011; Levin et al., 2012; Paramonov et
448 al., 2013; Liu et al., 2014), and is attributed to the enrichment in organic material of
449 sub-100 nm particles. Based on the derived κ values for each particle size and with
450 knowledge of the distinct species identified by the ACSM (organics, sulfate) and their
451 respective hygroscopicities, the volume fractions for organics and inorganics (mainly
452 ammonium sulfate) were estimated for each particle size. It occurs that indeed, 60 nm
453 particles are, on average, 89% composed of organics while the respective values for
454 80, 100 and 120 nm particles are 70, 50 and 41%. Most of the accumulation mode
455 particles result from condensation of secondary sulfates, nitrates and organics from
456 the gas phase and coagulation of smaller particles (Seinfeld and Pandis, 2006). In
457 order to examine the contribution of constituents from primary sources that are not
458 measured by the ACSM to the accumulation mode particles, we compared the mass
459 derived from the ACSM+BC and the integrated volume distribution from the SMPS
460 converted to mass. During the examined fire events, the ACSM+BC was on average
461 $68.6 \pm 19.3\%$ of the SMPS-derived mass. Therefore this is an indication that non-
462 refractory material neglected by the ACSM in the accumulation mode particles have
463 probably small influence on particle hygroscopicity. Accumulation mode particles can
464 also result from cloud processing. Based on cloud droplet calculations presented in a
465 subsequent section (Section 3.8) it appears that particles subject to atmospheric
466 processing would be present in a separate mode around 120 nm ($f_{s_{max}} \sim 0.08\%$).

467 Particles larger than 100 nm are usually more aged than the smaller particles and more
468 immediately associated with BB plumes and the atmospheric processing they undergo
469 (Kalivitis et al., 2015). The hygroscopicity parameter for 100 and 120 nm particles are
470 very similar and the fact that the variability in the respective chemical composition is
471 limited may indeed be attributed to cloud processing, while 80-nm particles are in
472 between the lowest and highest κ_{CCN} values, an indication of size-dependent chemical
473 composition of components with different hygroscopicities.

474 Figure 6 also shows that during the arrival of the biomass burning-laden air masses, κ
475 values of all particle size ranges within 0.2-0.3. This observation is consistent with
476 values observed from chamber experiments of fresh and aged biomass burning aerosol
477 and in-situ studies from the field. Engelhart et al. (2012) performed a study where 12
478 different biomass fuels commonly burnt in North American wildfires were used to
479 characterize their respective hygroscopicity. They found that while κ of freshly emitted
480 BBOA prior to photochemical aging covered a range from 0.06 to 0.6, after a few hours
481 of photochemical processing, the variability of biomass burning κ values from the
482 different fuels was reduced and hygroscopicity converged to a value of 0.2 ± 0.1
483 (Cerully et al., 2011; Engelhart et al., 2012). Based on the derived hygroscopicity
484 parameters for each particles size before and during the BB influence, it occurs that
485 smoke causes a relative decrease of κ in the order of 22% for 80 nm particles, 30.6%
486 for 100 nm particles and 30.9% for 120 nm particles on average for the four events
487 while κ for 60 nm particles deviate by only 14%.

488 During the fire events the contribution of organics and BC to the submicron aerosol
489 mass fraction increased significantly while the presence of sulfate declined. This is
490 expected to influence the CCN activity of the sampled aerosol particles as it would
491 cause variations in the inorganic and organic mass fractions. It has already been
492 established that the κ value of primary aerosol decreases as the organic mass fraction
493 of aerosol increases (Petters et al., 2009; Engelhart et al., 2012). With photochemical
494 aging, the increased oxygenation of the freshly emitted BBOA may influence the
495 hygroscopicity of the organic components, but the concurrent increase of the inorganic
496 fraction of the aerosol contributes to the observed increase of κ_{CCN} (inorganic content
497 vs aging).

498 To examine the impact of atmospheric processing and aging on the composition of the
499 sampled aerosol, we studied the chemical dispersion $\sigma(\kappa)$ of the hygroscopicity
500 parameter κ , expressed by the standard deviation of kappa around the most probable
501 hygroscopicity κ^* , and its dependence on particle size. As normal operation
502 uncertainties and the DMA transfer function can induce a broadening of $R_a(s)$ and $R_a(\kappa)$
503 and therefore contribute to $\sigma(\kappa)$, the inferred $\sigma(\kappa)$ contains a fairly constant instrument
504 offset and a time-dependent constituent that is representative of the real chemical
505 variability. This offset value, owing to the DMA transfer function and other instrument
506 limits has been calculated to be roughly 0.25 (Cerully et al. 2011). Table 1 shows the
507 calculated chemical dispersion, in terms of $\sigma(\kappa)/\kappa$, for the four fire events and the
508 measured particle sizes. It is immediately apparent that the chemical dispersion is
509 reduced with increasing particle size. 60-nm particles exhibit the highest dispersion
510 especially for the Chios fire, suggesting that the smaller particles are a mixture of
511 freshly-emitted BB particles and particles formed from the condensation of organics

512 during the transport from the fire location to Finokalia, as organics become less volatile
513 with atmospheric processing, increasing the chemical dispersion. The 80 and 100-nm
514 particles from the Chios fire have high $\sigma(\kappa)/\kappa$ values while the ones from Euboea and
515 Andros have considerably lower values, demonstrating the magnitude of the Chios fire
516 and the degree of atmospheric processing that has taken place. Finally, 120-nm
517 particles always have a low chemical dispersion, with $\sigma(\kappa)/\kappa$ values close to the
518 instrument limit. Nevertheless, the chemical dispersion of all particle sizes appears to
519 be influenced by the presence of BB as there is an average relative increase of $\sigma(\kappa)/\kappa$
520 values of 21, 28, 41 and 43% for 60, 80, 100 and 120 nm particles, respectively, before
521 and during the event. The increased chemical dispersion of particles smaller than 80
522 nm can be, therefore, attributed to the heterogeneity of sources of these particles
523 (which is also seen by CALIOP, Figure 3c) combined with lack of extensive cloud
524 processing because the particles are too small to activate in boundary layer clouds in
525 the region (Section 3.8). For larger particles, the chemical dispersion may be due to
526 mixing with other types of aerosol that are not identified by the ACSM; microphysical
527 processing such as condensational growth and cloud processing may be the reason
528 why they exhibit a smaller chemical dispersion than smaller particles. Indeed, the
529 surface area distributions (Figure S1 of the Supplement) peaks at around 200 nm
530 which means that condensation of SOA mass is most effective in that size range.
531 Coagulation/condensation continuously occurs together with any new source and NPF
532 during atmospheric transport (Triantafyllou et al., 2016; Kalkavouras et al., 2016), but
533 cloud processing mixes everything and makes it completely homogeneous at the
534 respective activation diameter that corresponds to each fire event. In terms of aerosol
535 microphysical processes, numerical simulations indicate that for half a day of aging
536 under moderately polluted conditions, coagulation has been found to internally mix
537 almost all particles above 0.2 μm , and smaller particles to a lesser extent (e.g.
538 Jacobson, 2002). Condensation, for the same time scale, increases the fractional
539 coating of small particles rather than large ones.

540

541

3.6 Particle growth factors during the fire events

542 From the concurrent HTDMA growth factor measurements at sub-saturated conditions
543 we calculated the corresponding κ_{HTDMA} values. During the focus period of the biomass
544 burning events as well as a few days before and after the events, the grand majority
545 of the HTDMA data exhibited unimodal distributions, indicating that all selected particle
546 fractions were internally mixed. Bimodal hygroscopicity distributions were only
547 observed during the arrival of the smoke plumes from the most intense events and
548 therefore are not taken into account for the comparison study between CFSTGC and
549 HTDMA-derived κ values. Average CFSTGC-derived κ_{CCN} values and HTDMA-derived
550 κ_{HTDMA} values for the selected particles sizes are given in Table 2. On average, κ_{HTDMA}
551 values are somewhat lower than the respective κ_{CCN} values for the smaller particles,
552 while the difference between them is larger for the larger particle sizes. Nevertheless,
553 both time series follow the same trend and values are consistent within $\pm 30\%$
554 ($\kappa_{HTDMA} = 0.854 \cdot \kappa_{CCN}$, $R^2 = 0.87$; Figure S2 in the supplement). Owing to non-ideality in
555 the aqueous phase, partial solubility of the organics and the existence of multiple

556 phases under subsaturated conditions, HTDMA-derived κ_{HTDMA} values may indeed be
557 lower than the corresponding CCN-derived ones. In the study of Wu et al. (2013), κ
558 derived from CCN measurements was also roughly 30% higher than that determined
559 from hygroscopic growth measurements. Similar effects are also seen for laboratory
560 generated aerosol composed of single and multiple compounds (Petters and
561 Kreidenweis, 2007). Apart from non-ideality solution effects, the presence of
562 surfactants produced during biomass burning events (Asa-Awuku et al., 2008) may
563 also increase the discrepancies between κ -HTDMA and κ -CCN (Ruehl et al., 2012).
564 Other studies as well note similar magnitude of difference between CFSTGC and
565 HTDMA-derived κ values (e.g. Prenni et al., 2007; Massoli et al., 2010; Cerully et al.
566 2011).

567 The probability distribution of growth factors in the HTDMA gives an independent
568 measure of particle mixing state. During the two most intense fire events (i.e. during
569 the Chios and Euboea fire) where the smoke plume had the least amount of transit
570 and atmospheric processing time, all sizes exhibited two different hygroscopic modes
571 (Tables 3 and 4; Figure S3 in the supplement). These distinct modes were not
572 observed during the other two events, owing to longer time of processing that allowed
573 for condensation growth and mixing of the populations. Figure 7 portrays in the left-
574 hand panels the $\overline{\kappa_{HTDMA}}$ (estimated using Equation 6) for the sampled particle sizes
575 during the Chios and Euboea fires. The right-hand panels show the respective particle
576 size distributions obtained by the concurrent SMPS measurements, revealing the
577 presence of different particle modes. It should be noted that values differ from the
578 respective κ_{CCN} values, under subsaturated conditions, because if some particles do
579 not grow inside the HTDMA they are directly assigned with a growth factor equal to
580 one (i.e. $\kappa=0$), subsequently reducing considerably the derived kappa value. These
581 hydrophobic particles are likely not fully counted by the CFSTGC and hence do not
582 contribute to the average κ_{CCN} . During the arrival of the smoke-influenced air masses,
583 there is a decrease in the hygroscopicity of all measured sizes. At the same time a
584 bimodal distribution was observed by the SMPS (far right panels), indicative of two
585 groups of particles, which can be partially due to the presence of freshly emitted
586 particles (i.e. smaller mode) in combination with larger, more processed ones. Adler
587 et al. (2011) had also observed a shift in the average mode diameter of size
588 distributions from 86 ± 8 nm for freshly-emitted BBOA to 114 ± 7 nm for processed BBOA.
589 This further supports the observed higher chemical dispersion in the smaller particle
590 sizes (Section 3.5).

591 A similar behavior when the sampled particles influenced by biomass burning were
592 exposed to sub-saturated conditions has been reported by Rissler et al. (2006). In
593 those measurements the hygroscopic growth of the sampled particles when exposed
594 to 90% RH showed that there was an external mixture of a nearly hydrophobic
595 ($g_{(RH)}=1.09$ for 100 nm particles) and a moderately hygroscopic ($g_{(RH)}=1.26$)
596 population. This reinforces our observations from the CCN measurements, where for
597 super-saturated conditions, the activation fraction of mainly the 60 nm particles
598 decreased significantly under influence of the smoke. A possible explanation why the
599 activation fractions of the other size ranges remain close to unity during the smoke
600 influence may result from the cloud processing of these sizes and their mixing with

601 background particles, contributing to their hygroscopicity and chemical dispersion. The
 602 overall characteristics are expected to be determined by the number fraction of the
 603 two modes in each size, combined with the occurrence of these two modes. If the
 604 presence of the bimodal samples is limited (less than 30%), then even though the
 605 fraction of the less hygroscopic mode may be as high as 45%, the overall activation
 606 fractions might not be influenced. For the first event (20-21/8) which was the most
 607 intense, the externally mixed samples represent almost 25% of the total sampled
 608 aerosol, with the occurrence of the bimodal samples increasing with increasing
 609 diameter (Table 3). It appears that in the bimodal samples the less hygroscopic mode
 610 initially dominates followed by a progressive dominance of the hygroscopic mode. It
 611 also appears that the increase in the less hygroscopic fraction coincides with the plume
 612 arrival time and the increase of the BBOA component, further supporting our findings
 613 of external mixing. During the second event (03-05/9) the bimodal samples increase,
 614 once more, with increasing diameter (5% for 60 nm to 28% for 120 nm particles). The
 615 less hygroscopic fraction in this case was dominant in approximately 33% of the
 616 samples, although this more hygroscopic mode had a κ_{HTDMA} value of 0.2 during the
 617 plume arrival time (Table 4). The more hygroscopic mode is therefore dominant in
 618 number for all sampled particles, which would explain that the activation fraction of
 619 the larger accumulation mode particles are not significantly affected by the presence
 620 of the less hygroscopic mode. On the other hand, the reason for the reduction of the
 621 activation fraction of 60-nm particles, apart from their hygroscopicity, can also be their
 622 different source and size, as during the events, the less hygroscopic mode is probably
 623 not activated, thus not detected by the CCN counter. This is not the case for the larger
 624 particles, as for example, 80-nm particles having a low $\kappa_{HTDMA}=0.06$ will still activate
 625 at the highest supersaturations sampled ($s=0.67\%$).

626

627 ***3.7 Inferring size-dependent chemical composition and organic*** 628 ***hygroscopicity***

629 Assuming that the total aerosol hygroscopicity can be represented as the sum of the
 630 contribution of the different aerosol components:

$$631 \quad \kappa = \sum_j \varepsilon_j \kappa_j \quad (7)$$

632 where ε_j and κ_j are the volume fraction and hygroscopicity parameters of each species,
 633 respectively (Petters and Kreidenweis, 2007). With the use of this equation, and by
 634 assuming that the aerosol is a mixture of an organic and inorganic component, with
 635 the inorganic component being represented by ammonium sulfate, the total measured
 636 hygroscopicity, can be expressed by the sum:

$$637 \quad \kappa = \varepsilon_{inorg} \kappa_{inorg} + \varepsilon_{org} \kappa_{org} \quad (8)$$

638 Prior studies at Finokalia (Bougiatioti et al. 2009; 2011) have determined $\kappa_{org}=0.158$
 639 and $\kappa_{inorg}=0.6$. Assuming this still applies and $\varepsilon_{inorg}+\varepsilon_{org}=1$, Equation 8 can be used to
 640 infer the volume fractions of organics and ammonium sulfate for the 4 different sizes,
 641 excluding the days of direct biomass burning influence. From this we obtain that 60
 642 nm particles, on average, are composed of 82% organics and 18% ammonium sulfate;
 643 80 nm particles, of 44% organics and 55% ammonium sulfate, and the larger particles

644 contain a much larger fraction of ammonium sulfate (67% and 78% for 100 and 120
645 nm particles, respectively). This reinforces our conclusion based on the hygroscopicity
646 measurements that the smaller particles are mostly composed of organic material.
647 These observations are in agreement with similar observations reported by Bezantakos
648 et al. (2013) in the region of the northern Aegean Sea.

649 The above approach can also be applied to the data from the fire events, as follows:
650 we use only the larger size (120 nm) as from the former CCN studies in the area it was
651 established that the hygroscopicity of the larger particles is close to the “bulk”
652 hygroscopicity of the sampled aerosol (PM₁), which is constrained from the ACSM
653 measurements (Bougiatioti et al., 2011). To evaluate the importance of the
654 assumptions made in inferring the organic hygroscopicity from chemical composition,
655 κ_{org} was additionally determined by applying Equation 8, for the 120 nm particles,
656 where a set of κ equations is produced (n=228). Multivariable regression analysis
657 within the excel environment is subsequently applied in order to determine the organic
658 and inorganic component of the total hygroscopicity during the fire events. Based on
659 the results, $\kappa_{inorg}=0.61\pm0.03$ and $\kappa_{org}=0.137\pm0.02$, values which are very similar to
660 values determined by Bougiatioti et al. (2009; 2011). The confidence level is 95% and
661 the resulting fit has an $R^2=0.91$ and p-values are smaller than $8\cdot10^{-7}$ for both
662 components.

663 Taking the analysis one step further, we attempt a source apportionment of the
664 organic hygroscopicity, by its attribution to different factors. Positive Matrix
665 Factorization (PMF) analysis was applied to the time series of data under the direct
666 influence from biomass burning. A detailed discussion of the PMF results can be found
667 in Bougiatioti et al. (2014). During the focus period, 3 subtypes of organic aerosol (OA)
668 were identified, namely biomass burning OA (BBOA), an OOA associated with biomass
669 burning (OOA-BB) and a highly oxygenated OOA, having a relative contribution of 22,
670 32 and 46%, respectively. With the chemical composition measurements of the ACSM
671 applied to the larger particle size (120 nm) combined with the respective κ_{CCN} we use
672 the following equation to determine the hygroscopicity parameter of each factor:

$$673 \quad \kappa = (1 - \varepsilon_{org})\kappa_{inorg} + \varepsilon_{BBOA}\kappa_{BBOA} + \varepsilon_{OOA-BB}\kappa_{OOA-BB} + \varepsilon_{OOA}\kappa_{OOA} \quad (9)$$

674 Once again a set of 228 κ equations is produced and multivariable regression analysis
675 is applied in order to deconvolve the organic hygroscopicity to its 3 subtypes. The
676 confidence level once more is 95% and the resulting fit has an $R^2=0.93$, with p-values
677 smaller than 0.001. It occurs that $\kappa_{inorg}=0.62\pm0.04$, $\kappa_{BBOA}=0.057\pm0.07$, κ_{OOA-}
678 $BB=0.138\pm0.11$ and $\kappa_{OOA}=0.169\pm0.09$. As the occurrence of two modes of different
679 hygroscopicity seen by the HTDMA during the arrival of the smoke coincide with the
680 identification of BBOA by the ACSM, it is interesting to see that the inferred
681 hygroscopicity for the freshly-emitted BBOA is very close to the hygroscopicity
682 obtained by the HTDMA for the less hygroscopic component when two particle
683 populations were present during the events (Tables 3 and 4, Section 3.6). When
684 comparing the obtained hygroscopicity with the level of oxidation of each factor
685 (O:C=0.2 for BBOA, 0.9 for OOA-BB and 1.2 for OOA; Bougiatioti et al., 2014) it occurs
686 that the less hygroscopic component is also the least oxygenated and that
687 hygroscopicity increases with increasing O:C ratio. The calculated values are also

688 comparable to the κ obtained by Chang et al. (2010) for the oxygenated organic
689 component (OOA-1, OOA-2 and BBOA) of rural aerosol ($\kappa_{ox}=0.22\pm 0.04$). They also
690 found increased hygroscopicity with increasing ageing and degree of oxidation.
691 Furthermore, the total organic hygroscopicity is very similar to that of the processed
692 organic aerosol components, which make up almost 80% of the organic aerosol.
693 Finally, based on the derived hygroscopicities for the BBOA and the processed BBOA
694 (OOA-BB), it seems that the biomass burning organic aerosol becomes more
695 hygroscopic, by almost a factor of two, with atmospheric processing.
696 Using the average diurnal profiles obtained from the PMF analysis combined with the
697 corresponding mass fractions of each component and the inferred hygroscopicity
698 parameter of each, we estimated the contribution of each factor to the overall κ_{org} and
699 the total aerosol hygroscopicity. Figure 8 presents the resulting diurnal profiles from
700 which it is clear that the grand majority of the organic hygroscopicity originates from
701 the aged, very oxidized OOA. BBOA contributes around 7% to the organic
702 hygroscopicity (2.2% to the overall aerosol hygroscopicity), which is small but not
703 negligible, as it can be seen that when the BBOA contribution is the highest, there is
704 an important decrease in the κ_{org} . Overall, organic aerosol associated with biomass
705 burning can account for almost 35% of the organic hygroscopicity. By using the
706 approach of Guo et al. (2015) where particle water is predicted using meteorological
707 observations (relative humidity, temperature), aerosol composition and
708 thermodynamic modeling (ISORROPIA-II; Fountoukis and Nenes, 2007), the LWC
709 associated with the organic fraction is calculated. We find that although the freshly-
710 emitted BBOA contributes merely 1.2% to the total organic water of the aerosol, the
711 contribution of the processed OOA-BB is almost 33%. It is therefore clear that in the
712 presence of biomass burning aerosol, both aerosol hygroscopicity and LWC may be
713 influenced, thus affecting the overall direct and indirect aerosol radiative effects.

714

715 **3.8 BB influence on droplet formation**

716 The direct microphysical link between aerosol and clouds is the activation process,
717 where a fraction of the aerosol contained within an ascending cloud parcel experiences
718 unconstrained growth and activates to form cloud droplets. State of the art cloud
719 droplet parameterizations (Ghan et al., 2011; Morales Betancourt and Nenes, 2014)
720 can accurately and rapidly calculate the droplet number (N_d) and maximum
721 supersaturation (S_{max}) that would form in a cloud given knowledge of the aerosol
722 distribution, composition and updraft velocity. Using the aerosol and hygroscopicity
723 observations from all four BB events, we calculate the droplet number and
724 supersaturation for clouds forming in the vicinity of Finokalia, using the droplet
725 parameterizations based on the “population splitting concept” of Nenes and Seinfeld
726 (2003), later improved by Barahona et al., (2010) and Morales and Nenes (2014). In
727 the calculations of droplet number, the size distribution is represented by the sectional
728 approach, derived directly from the SMPS distribution files. Values of updraft velocity
729 are not known for Finokalia, but are obtained from the WRF regional model applied to
730 late summer conditions (Kalkavouras et al., 2016); simulations suggest that the
731 distribution of vertical velocities in the boundary layer around Finokalia displays a

732 spectral dispersion of $\sigma_w = 0.2\text{-}0.3 \text{ m s}^{-1}$ around a mean average value of 0.3. These
733 values are generally consistent with vertical velocities observed in marine boundary
734 layers (e.g., Meskhidze et al., 2005; Ghate et al., 2011). Given this, we can employ
735 the characteristic velocity approach of Morales and Nenes (2010) when applying the
736 droplet parameterization to obtain velocity PDF-averaged values of CDNC and S_{max} . As
737 a sensitivity test, we also consider calculations for a convective boundary layer ($\sigma_w =$
738 0.6 m s^{-1}). The calculation of PDF-averaged values of CDNC and S_{max} is carried out for
739 every distribution of aerosol number and composition measured for all four biomass
740 burning events (5-min resolution distributions from the SMPS measurements for at
741 least two days for each event). Results of all the calculations are shown in Figure 9.
742 As a reference, the time series of the BBOA component is also portrayed.
743 For all events, the arrival of the smoke plume is followed by a considerable depression
744 in the maximum supersaturation (relative average decrease (11.9 ± 2.7)% for $\sigma_w = 0.3$
745 ms^{-1} and (18 ± 5.9)% for $\sigma_w = 0.6 \text{ m s}^{-1}$) that develops in clouds. This is a result of the
746 enhanced competition for water vapor during cloud droplet formation for clouds
747 affected by biomass burning smoke. The negative feedback of aerosol on
748 supersaturation partially mitigates the observed increases in CCN to the point where
749 clouds are highly insensitive to the large aerosol concentration increases (Moore et al.,
750 2013; Zamora et al., 2016). As expected, increases in the updraft velocity ($\sigma_w = 0.6$
751 m s^{-1}) reduces the competition of CCN for water vapor, allowing S_{max} to increase, by
752 almost 30%. The respective perturbation of N_d from BB influences by doubling the
753 updraft velocity increases to 54% on average (from 9.3% to 24.2% for Chios, from
754 8.5% to 15.2% for Croatia, from 11% to 18.8% for Euboea and from 4% to 13.8%
755 for Andros). The low supersaturations developed in BB-influenced clouds (here, as low
756 as 0.06%) shifts the size of particles affected by cloud processing to the largest
757 particles (cutoff diameters before and during the Chios intense event were on average
758 133 and 109 nm, respectively, while during the other events they were on average
759 154.8 and 129.3 nm, respectively). Interestingly, the notable drop in chemical
760 dispersion in the 100-120 nm particle sizes are consistent with the notion that cloud
761 processing would considerably enhance their degree of internal mixing.
762 The degree to which BB influences N_d does not depend only on the value of updraft
763 velocity and the intensity of the BB event; it also depends on the background aerosol.
764 This is because the background preconditions the clouds and determines the levels of
765 supersaturation that develops prior to the arrival of the BB aerosol. Highly polluted
766 background generally means larger insensitivity of N_d to BB. This is shown clearly in
767 Figure 10, which presents the droplet number concentration (top panel) and cloud
768 maximum supersaturation (bottom panel) for each fire event as a function of BB
769 influence, expressed by the sum of BBOA and OOA-BB ACSM factors. From the figure
770 one can clearly see that when the background levels aerosol decreases (indicated by
771 the lower N_d and higher S_{max} at the low end of BB factor concentrations, which is
772 characteristic of the Coatia and Chios fires), N_d responds to increases in BB, up to the
773 point where the clouds become "saturated" with aerosol (with a supersaturation
774 around 0.08% and below, indicated by the shaded areas in Figure 10) and are
775 insensitive to additional increases in BB. Euboea and Andros fires already have a high
776 background, so the cloud droplet number is relatively insensitive to BB influence.

777 Finally, we estimated the relative contribution of chemical composition (from κ) and
 778 aerosol number concentration to the N_d , expressed by the average of the partial
 779 derivatives of dN_d/dN_a and dN_d/dN_κ and using the following equations:

$$780 \quad \sigma^2 N_d = \sigma N_a \frac{\overline{\partial N_d}}{\partial N_a} + \sigma \kappa \frac{\overline{\partial N_d}}{\partial N_\kappa} \quad (10)$$

781 where σ^2 is the variance of the droplet number (N_d), σN_a is the standard deviation of
 782 the total aerosol number and $\sigma \kappa$ is the standard deviation of the hygroscopicity
 783 parameter. The relative contribution of each one of the total aerosol number (εN_a) and
 784 hygroscopicity parameter ($\varepsilon \kappa$) to the droplet number is estimated by:

$$785 \quad \varepsilon \kappa_{N_d} = \sigma \kappa \frac{\overline{\partial N_d}}{\partial N_\kappa} \frac{dN_\kappa}{\sigma^2 N_d} \quad (11)$$

$$786 \quad \varepsilon N_{aNd} = \sigma N_a \frac{\overline{\partial N_d}}{\partial N_a} \frac{\partial N_a}{\sigma^2 N_d} \quad (12)$$

787 The results provided in Table 5 demonstrate that there are differences between the
 788 fire events, which can be attributed to the intensity of each event and thus the resulting
 789 concentrations, and the distance from the fire, thus the mixing and dilution during
 790 transport. The highest variance in N_d was calculated for the Andros event, which
 791 exhibited the lowest variability in $N_{aerosol}$ and the lowest variance was calculated for the
 792 Chios, followed by the Croatia event, which exhibited a variability in $N_{aerosol}$ of more
 793 than 1500 particles (cm^{-3}). From the relative contribution of the total aerosol number
 794 and chemical composition to N_d , it can be seen that the closest the fire event is, the
 795 largest the contribution of aerosol number to the potential CDNC. As we move further
 796 away (e.g. Chios and Croatia) and the distance increases, the influence of the chemical
 797 composition becomes increasingly important, given the decrease of concentrations
 798 and dilution during transport.

799

800 **4. Summary and Conclusions**

801 This study provides CCN concentrations, subsaturated hygroscopicity, mixing state of
 802 size-selected aerosol particles and their impact on cloud formation in air masses
 803 influenced by summer biomass burning (BB) events in the eastern Mediterranean. The
 804 uniqueness of the dataset examined lies in nature of the fires, where smoke is mostly
 805 generated from isolated fires and subsequently transported and aged from a few hours
 806 to days before sampling. The presence of smoke in the most intense events is clearly
 807 identified by CALIPSO lidar remote sensing and the MODIS FIRMS product, while
 808 chemical markers and backtrajectory analysis confirm the influence of BB in every
 809 event. During each event, the contribution of organics and BC increased significantly
 810 while the concentration of sulfates decreased. This is shown to affect the
 811 hygroscopicity as well as the mixing state of the particles. The fire events had a direct
 812 influence on the total particle (CN) and CCN concentrations across all sizes; particle
 813 sizes larger than 100 nm exhibited an increase in absolute number of more than 50%

814 and up to 30% for particles in the 60-80 nm range. The fraction of the smaller particles
815 acting as CCN even at the highest level of measured supersaturation (0.6% s),
816 however, went significantly below unity in the presence of smoke. This and the overall
817 value of hygroscopicity indicate that less CCN-active organic compounds are the
818 dominant component of 60-nm and smaller particles (up to 82% of mass), while
819 particles larger than 100 nm contain a much larger fraction of ammonium sulfate. The
820 subsaturated hygroscopicity measurements confirm this, as 60-nm particles exhibited
821 the lowest hygroscopic growth.

822 During the arrival of the biomass-burning-laden air masses, the average hygroscopicity
823 parameters of all particle sizes converged to values between 0.2-0.3, which can be
824 attributed to different chemical composition of all particles during these events,
825 compared to background conditions. The hygroscopicity distributions and chemical
826 dispersion analysis of the CCN data clearly show that smaller particles exhibit higher
827 chemical diversity (variance in hygroscopicity equal to 0.15 κ units) than larger
828 particles (variance in hygroscopicity less than 0.1 κ units) . This size-dependent mixing
829 state may reflect the presence of different aerosol sources with characteristic sizes
830 (e.g. sea-salt, pollution in addition to BB) and size-dependent chemical composition;
831 the fact that smaller particles are less mixed than larger particles- together with that
832 the background aerosol is composed of a large mode with a distinct chemical
833 composition- suggests that the smaller particles are an external mixture of freshly
834 emitted and secondarily formed particles that retain a large degree of mixing. Larger
835 particles are further aged and subject to coagulation, condensation of secondary
836 species and cloud processing, all of which tend to homogenize the aerosol. However,
837 two aerosol populations with distinct hygroscopicity were seen even at the largest sizes
838 sampled during the most intense fire events. Nevertheless, their occurrence is limited
839 and the overall activation of larger particles appears to be unaffected by the presence
840 of these two populations. In terms of cloud processing effects, the largest particles
841 that are predicted to form droplets in clouds in the vicinity of the sampling site indeed
842 exhibit the lowest chemical dispersion. This supports the assumption of external mixing
843 for smaller particles originating from biomass burning having decreased activation
844 fractions and provides a plausible explanation of why larger particles appear, based on
845 their activation fractions, not to be affected as far as their CCN-activity is concerned.
846 Using multivariable regression analysis and the volume fractions of organics and
847 ammonium sulfate for the different particle sizes, we inferred the hygroscopicity of the
848 organic fraction and found it equal to 0.115 ± 0.017 , which is consistent with published
849 values from the literature. Using the results obtained from the source apportionment
850 of the organic fraction we were able to deconvolve the organic hygroscopicity to its 3
851 subtypes. The hygroscopicity of freshly-emitted BBOA was found to be around 0.06,
852 while the hygroscopicity of atmospherically-processed BBOA and highly oxidized
853 organic aerosol was found to be 0.14 and 0.17, respectively. The inferred
854 hygroscopicity of each component and its oxidation state are in line with the overall
855 organic aerosol values observed. From this and the trends of each factor with
856 atmospheric age we conclude that the organic fraction of biomass burning aerosol
857 becomes more hygroscopic with atmospheric aging. Overall, organic aerosol
858 associated with biomass burning (freshly emitted and processed) can account for 10%

859 of the total aerosol hygroscopicity (2.2 and 7.6% for BBOA and OOA-BB, respectively).
860 For the observed levels of relative humidity, and amount of each organic aerosol factor,
861 we estimate that BBOA and OOA-BB contribute anywhere between 1.2 and 32.6% of
862 the total organic water of the aerosol.

863 Towards understanding the impacts of the observed BB on clouds, we study the
864 behavior of cloud droplet formation for typical boundary layer conditions. For this, we
865 apply a state of the art cloud droplet formation parameterization to the observations,
866 assuming typical values of updraft velocity for marine boundary layer clouds. We find
867 that the very high concentrations of CCN during the influence of BB events tend to
868 promote the competition for cloud water vapor, and substantially depresses the cloud
869 supersaturation down to very low levels (even as low as 0.06%). As a result, only the
870 largest particles, from 110-150 nm in diameter and above, can activate to form cloud
871 droplets. This also means that droplet number becomes highly insensitive to changes
872 in aerosol in the presence of BB; indeed clouds influenced by BB exhibit a relative
873 decrease in maximum supersaturation by 12% while at the same time, BB augments
874 the potential droplet number by 8.5%. These results also support the chemical
875 dispersion/mixing state analysis of the CCN data, as only the largest aerosol sizes
876 sampled activate and are exposed to cloud processing. Based on the average
877 sensitivity of droplet number to changes in aerosol number and composition, and
878 observed variances thereof, we attribute the relative contribution of chemical
879 composition and total aerosol number to the variance of droplet number. We find that
880 the distance from the source is a key parameter that governs the importance of each
881 parameter, with the influence of the chemical composition becoming increasingly
882 important (controlling up to 25% of the droplet number variability) with growing
883 distance from the source. Close to sources, the exclusive majority (98% and above)
884 of the predicted droplet number variability is attributed to aerosol number variations.
885 Therefore, although BB burning may strongly elevate CCN numbers, the relative
886 impacts on cloud droplet number (compared to background levels) is eventually limited
887 by water vapor availability and depends on the aerosol levels associated with the
888 background.

889

890 **Acknowledgments**

891 The work of A. Bougiatioti, A. Papayannis, P. Kokkalis was supported by the "MACAVE"
892 research project and the work of N. Kalivitis by the "FRONT" research project, which
893 are implemented within the framework of the action Supporting of Postdoctoral
894 Researchers of the Operational Program Education and Lifelong Learning (action's
895 beneficiary: General Secretariat for Research and Technology), and is co-financed by
896 the European Social Fund (ESF) and the Greek State. This research has also been co-
897 financed by the European Union (European Social Fund – ESF) and Greek national
898 funds through the Operational Program "Education and Lifelong Learning" of the
899 National Strategic Reference Framework (NSRF) - Research Funding Program:
900 THALES, Investing in knowledge society through the European Social Fund. The
901 financial support by the European Community through the ACTRIS Research
902 Infrastructure Action and Bacchus project under the 7th Framework Programme (Grant
903 Agreements no 262254 and 603445, respectively) are gratefully acknowledged. AN

904 acknowledges support from a Georgia Power Faculty Scholar Chair and a Cullen-Peck
905 Faculty Fellowship. This study contributes to ChArMEx Work Packages 2 and 4,
906 respectively on chemical aging and regional aerosol-climate interactions.
907

908 **References**

- 909 Adler, G., Flores, J.M., Abo Riziq, A., Borrmann, S., and Rudich, Y.: Chemical, physical, and
910 optical evolution of biomass burning aerosols: a case study, *Atmos. Chem. Phys.*, 11, 1491-
911 1503, doi:10.5194/acp-11-1491-2011, 2011.
- 912 Andreae, M. O., Rosenfeld, D., Artaxo, P., Costa, A. A., Frank, G. P., Longo, K. M., and Silva
913 Dias, M. A. F.: Smoking rain clouds over the Amazon, *Science*, 303, 1337–1342, 2004.
- 914 Asa-Awuku, A., Nenes, A., Sullivan, A.P., Hennigan, C.J. and Weber, R.J.: Investigation of molar
915 volume and surfactant characteristics of water-soluble organic compounds in biomass
916 burning aerosol, *Atmos. Chem. Phys.*, 8, 799-812, 2008.
- 917 Barahona, D., West, R.E.L., Stier, P., Romakkaniemi, S., Kokkola, H., and A. Nenes:
918 Comprehensively Accounting for the Effect of Giant CCN in Cloud Activation
919 Parameterizations, *Atmos. Chem. Phys.*, 10, 2467-2473, 2010.
- 920 Bezantakos, S., K. Barmounis, M. Giamarelou, E. Bossioli, M. Tombrou, N. Mihalopoulos, K.
921 Eleftheriadis, J. Kalogiros, J.D. Allan, A. Bacak, C.J. Percival, H. Coe and G. Biskos: Chemical
922 Composition and Hygroscopic Properties of Aerosol Particles over the Aegean Sea, *Atmos.*
923 *Chem. Phys.*, 13 (22), 11595–608, doi:10.5194/acp-13-11595-2013, 2013.
- 924 Biskos, G., D. Paulsen, L. M. Russell, P. R. Buseck, and S. T. Martin: Prompt Deliquescence and
925 Efflorescence of Aerosol Nanoparticles, *Atmos. Chem. Phys.* 6, 4633–42, 2006.
- 926 Bougiatioti, A., Fountoukis, C., Kalivitis, N., Pandis, S.N., Nenes, A., and Mihalopoulos, N.: Cloud
927 condensation nuclei measurements in the marine boundary layer of the eastern
928 Mediterranean: CCN closure and droplet growth kinetics, *Atmos. Chem. Phys.*, 9, 7053-7066,
929 2009.
- 930 Bougiatioti, A., Nenes, A., Fountoukis, C., Kalivitis, N., Pandis, S.N., and Mihalopoulos, N.: Size-
931 resolved CCN distributions and activation kinetics of aged continental and marine aerosol,
932 *Atmos. Chem. Phys.*, 11, 8791-8808, doi:10.5194/acp-11-8791-2011, 2011.
- 933 Bougiatioti, A., Stavroulas, I., Kostenidou, E., Zarnpas, P., Theodosi, C., Kouvarakis, G.,
934 Canonaco, F., Prévôt, A.S.H., Nenes, A., Pandis, S.N., and Mihalopoulos, N.: Processing of
935 biomass-burning aerosol in the eastern Mediterranean during summertime, *Atmos. Chem.*
936 *Phys.*, 14, 4793-4807, doi:10.5194/acp-14-4793-2014, 2014.
- 937 Carlton, A. G. and Turpin, B. J.: Particle partitioning potential of organic compounds is highest
938 in the Eastern US and driven by anthropogenic water, *Atmos. Chem. Phys.*, 13, 10203–
939 10214, doi:10.5194/acp-13-10203-2013, 2013.
- 940 Cerully, K.M., Raatikainen, T., Lance, S., Tkacik, D., Tiitta, D., Petäjä, T., Ehn, M., Kulmala, M.,
941 Wornson, D.R., Laaksonen, A., Smith, J.N. and Nenes, A.: Aerosol hygroscopicity and CCN
942 activation kinetics in a boreal forest environment during the 2007 EUCAARI campaign,
943 *Atmos. Chem. Phys.*, 11, 12369-112386, doi:10.5194/acp-11-12369-2011, 2011.
- 944 Cerully, K. M., Bougiatioti, A., Hite Jr., J. R., Guo, H., Xu, L., Ng, N. L., Weber, R., and Nenes,
945 A.: On the link between hygroscopicity, volatility, and oxidation state of ambient and water-
946 soluble aerosol in the Southeastern United States, *Atmos. Chem. Phys. Discuss.*, 14, 30835-
947 30877, doi:10.5194/acpd-14-30835-2014, 2014.
- 948 Chang, R. Y-W., Slowik, J. G., Shantz, N. C., Vlasenko, A., Liggio, J., Sjostedt, S. J., Leaitch, W.
949 R., and Abbatt, J. P. D.: The hygroscopicity parameter (κ) of ambient organic aerosol at a
950 field site subject to biogenic and anthropogenic influences: relationship to degree of aerosol
951 oxidation, *Atmos. Chem. Phys.*, 10, 5047–5064, doi:10.5194/acp-10-5047-2010, 2010.
- 952 Dusek, U., Frank, G. P., Curtius, J., Drewnick, F., Schneider, J., Kürten, A., Rose, D., Andreae,
953 M. O., Borrmann, S., and Pöschl, U.: Enhanced organic mass fraction and decreased
954 hygroscopicity of cloud condensation nuclei (CCN) during NPF events, *Geophys. Res. Lett.*,
955 37, L03804, doi:10.1029/2009GL040930, 2010.

956 Engelhart, G. J., Hennigan, C. J., Miracolo, M. A., Robinson, A. L., and Pandis, S. N.: Cloud
957 condensation nuclei activity of fresh primary and aged biomass burning aerosol, *Atmos.*
958 *Chem. Phys.*, 12, 7285-7293, doi:10.5194/acp-12-7285-2012, 2012.

959 Fountoukis, C. and Nenes, A.: ISORROPIA II: a computationally efficient thermodynamic
960 equilibrium model for K^+ - Ca^{2+} - Mg^{2+} - NH_4^+ - SO_4^{2-} - NO_3^- - Cl^- - H_2O aerosols, *Atmos. Chem. Phys.*,
961 7, 4639–4659, doi:10.5194/acp-7-4639-2007, 2007.

962 Fountoukis, C. and A. Nenes, A.: Continued Development of a Cloud Droplet Formation
963 Parameterization for Global Climate Models, *J. Geophys. Res.*, 110, D11212,
964 doi:10.1029/2004JD005591, 2005.

965 Ghan, S.J., Abdul-Razzak, H., Nenes, A., Ming, Y., Liu, X., Ovchinnikov, M., Shipway, B.,
966 Meskhidze, N., Xu, J., Shi, X.: Droplet Nucleation: Physically-based Parameterization and
967 Comparative Evaluation, *J. Adv. Model. Earth Syst.*, 3, doi:10.1029/2011MS000074, 2011.

968 Ghate, V.P., Miller, M.A., and DiPreto, L.: Vertical velocity structure of marine boundary layer
969 trade wind cumulus clouds, *J. Geophys. Res.*, 116, D16, 2156-2202,
970 doi:10.1029/2010JD015344, 2011.

971 Guo, H., Xu, L., Bougiatioti, A., Cerully, K.M., Capps, S.L., Hite, J.R.Jr., Carlton, A.G., Lee, S.-
972 H., Bergin, M.H., Ng, N.L., Nenes, A., and Weber, R.J.: Fine-particle water and pH in the
973 southeastern United States, *Atmos. Chem. Phys.*, 15, 5211-5228, doi:10.5194/acp-15-5211-
974 2015, 2015.

975 Healy, R.M., Riemer, N., Wenger, J.C., Murphy, M., West, M., Poulain, L., Wiedensohler, A.,
976 O'Connor, I.P., McGillicuddy, E., Sodeau, J.R., and Evans, G.E.: Single particle diversity and
977 mixing state measurements, *Atmos. Chem. Phys.*, 14, 6289-6299, doi:10.5194/acp-14-
978 6289-2014, 2014.

979 Hildebrandt, L., Engelhart, G. J., Mohr, C., Kostenidou, E., Lanz, V. A., Bougiatioti, A., DeCarlo,
980 P. F., Prevot, A. S. H., Baltensperger, U., Mihalopoulos, N., Donahue, N. M., and Pandis, S.
981 N.: Aged organic aerosol in the Eastern Mediterranean: the Finokalia Aerosol Measurement
982 Experiment – 2008, *Atmos. Chem. Phys.*, 10, 4167-4186, doi:10.5194/acp-10-4167-2010,
983 2010.

984 Jacobson, M.Z.: Analysis of aerosol interactions with numerical techniques for solving
985 coagulation, nucleation, condensation, dissolution, and reversible chemistry among multiple
986 size distributions, *J. Geophys. Res. Atmospheres*, 107, D19, AAC 2-1-AAC 2-23, 2002.

987 Kalivitis, N., Gerasopoulos, E., Vrekoussis, M., Kouvarakis, G., Kubilay, N., Hatzianastassiou, N.,
988 Vardavas, I., and Mihalopoulos, N.: Dust transport over the eastern Mediterranean derived
989 from Total Ozone Mapping Spectrometer, Aerosol Robotic Network, and surface
990 measurements, *J. Geophys. Res.-Atmos.*, 112, D03202, doi:10.1029/2006JD007510, 2007.

991 Kalivitis, N., Kerminen, V.-M., Kouvarakis, G., Stavroulas, I., Bougiatioti, A., Nenes, A.,
992 Manninen, H.E., Petäjä, T., Kulmala, M., and Mihalopoulos, N.: Atmospheric new particle
993 formation as source of CCN in the Eastern Mediterranean marine boundary layer, *Atmos.*
994 *Chem. Phys.*, 15, 9203-9215, doi:10.5194/acpd-15-9203-2015, 2015.

995 Kalkavouras, P., Bossioli, E., Bezantakos, S., Bougiatioti, A., Kalivitis, N., Stavroulas, I.,
996 Kouvarakis, G., Protonotariou, A.P., Dandou, A., Biskos, G., Nenes, A., Mihalopoulos, N.,
997 and Tombrou, M.: Regional variability of gaseous and particulate species and impacts on
998 cloud formations at the South Aegean Sea during the Etesians, accepted for publication in
999 *Atmos. Chem. Phys. Discuss.* (acp-2016-330).

1000 Kanakidou, M., Seinfeld, J.H., Pandis, S.N., Barnes, I., Dentener, F.J., Facchini, M.C., Van
1001 Dingenen, R., Ervens, B., Nenes, A., Nielsen, C.J., Swietlicki, E., Putaud, J.P., Balkanski, Y.,
1002 Fuzzi, S., Horth, J., Moortgat, G.K., Winterhalter, R., Myrhe, C.E.L., Tsigaridis, K., Vignati,
1003 E., Stephanou, E.G., and Wilson, J.: Organic aerosol and global climate modeling: a review,
1004 *Atmos. Chem. Phys.*, 5, 1053-1123, 2005.

1005 Kaufman, Y.J., and Remer, L.A.: Detection of forests using MID-IR reflectance-An application
1006 for aerosol studies, *IEEE Trans. Geosci. Remote Sensing*, 32 (3), 672-683, 1994.

1007 Knutson, E.O., and Whitby, K.T.: Aerosol classification by electric mobility: Apparatus, theory,
1008 and applications, *J. Aerosol Sci.*, 6, 443-451, 1975.

1009 Kyzirakos, K., M. Karpathiotakis, G. Garbis, C. Nikolaou, K. Bereta, I. Papoutsis, T. Herekakis,
1010 D. Michail, M. Koubarakis, C. Kontoes, Wild fire monitoring using satellite images, ontologies
1011 and linked geospatial data, *Web Semantics: Science, Services and Agents on the World Wide*
1012 *Web*, 24, 18-26, 2014.

1013 Lance, S.: Quantifying compositional impacts of ambient aerosol on cloud droplet formation,
1014 Published Doctoral Thesis, Available at [http://etd.gatech.edu/theses/available/etd-](http://etd.gatech.edu/theses/available/etd-11132007)
1015 [11132007](http://etd.gatech.edu/theses/available/etd-11132007) 175217/unrestricted/lance_sara_m_200712_phd[1].pdf, 2007.

1016 Lance, S., Raatikainen, T., Onasch, T., Worsnop, D. R., Yu, X.-Y., Alexander, M. L., Stolzenburg,
1017 M. R., McMurry, P. H., Smith, J. N., and A. Nenes: Aerosol mixing-state, hygroscopic growth
1018 and cloud activation efficiency during MIRAGE 2006, *Atmos. Chem. Phys.*, 13, 5049–5062,
1019 2013.

1020 Levin, E. J. T., Prenni, A. J., Petters, M. D., Kreidenweis, S. M., Sullivan, R. C., Atwood, S. A.,
1021 Ortega, J., DeMott, P. J., and Smith, J. N.: An annual cycle of size-resolved aerosol
1022 hygroscopicity at a forested site in Colorado, *J. Geophys. Res.*, 117, D06201,
1023 doi:10.1029/2011JD016854, 2012.

1024 Liu, H. J., Zhao, C. S., Nekat, B., Ma, N., Wiedensohler, A., van Pinxteren, D., Spindler, G.,
1025 Müller, K., and Herrmann, H.: Aerosol hygroscopicity derived from size-segregated chemical
1026 composition and its parameterization in the North China Plain, *Atmos. Chem. Phys.*, 14,
1027 2525–2539, doi:10.5194/acp-14-2525-2014, 2014.

1028 Mamouri, R.E., V. Amiridis, A. Papayannis, E. Giannakaki, G. Tsaknakis, and D.S. Balis,
1029 Validation of CALIPSO space-borne derived aerosol vertical structures using a ground-based
1030 lidar in Athens, Greece, *Atmos. Meas. Techn.*, 2, 513-522, 2009.

1031 Mamouri, R.E., Papayannis, A., Amiridis, V., Müller, V., Kokkalis, P., Rapsomanikis, S.,
1032 Karageorgos, E. T., Tsaknakis, G., Nenes, A., Kazadzis S., and Remoundaki, E.: Multi-
1033 wavelength Raman lidar, sunphotometric and aircraft measurements in combination with
1034 inversion models for the estimation of the aerosol optical and physico-chemical properties
1035 over Athens, Greece, *Atmos. Meas. Tech.*, 5, 1793-1808, doi:10.5194/amt-5-1793-2012,
1036 2012.

1037 Massoli, P., Lambe, A. T., Ahern, A. T., Williams, L. R., Ehn, M., Mikkilä, J., Canagaratna, M.R.,
1038 Brune, W. H., Onasch, T. B., Jayne, J. T., Petäjä, T., Kulmala, M., Laaksonen, A., Kolb, C.E.,
1039 Davidovits, P., and Worsnop, D. R.: Relationship between aerosol oxidation level and
1040 hygroscopic properties of laboratory generated secondary organic aerosol (SOA) particles,
1041 *Geophys. Res. Lett.*, 37, L24801, doi:10.1029/2010GL045258, 2010.

1042 Meskhidze, N., A. Nenes, Conant, W. C., and Seinfeld, J.H.: Evaluation of a new Cloud Droplet
1043 Activation Parameterization with In Situ Data from CRYSTAL-FACE and CSTRIFE, *J. Geoph.*
1044 *Res.*, 110, D16202, doi:10.1029/2004JD005703, 2005.

1045 Mihalopoulos, N., Stephanou, E., Kanakidou, M., Pilitsidis, S., and Bousquet, P.: Tropospheric
1046 aerosol ionic composition above the Eastern Mediterranean area, *Tellus*, **49B**, 314-326,
1047 1997.

1048 Moore, R.H. and Nenes, A.: Scanning Flow CCN Analysis - A Method for Fast Measurements of
1049 CCN Spectra, *Aer.Sci.Tech.*, 43, 1192-1207, 2009.

1050 Moore, R.H., Cerully, K., Bahreini, R., Brock, C.A., Middelbrook, A.M., and Nenes, A.:
1051 Hygroscopicity and composition of California CCN during summer 2010, *J. Geophys. Res.*,
1052 117, D00V12, doi:10.1029/2011JD017352, 2012a.

1053 Moore, R.H., Raatikainen, T., Langridge, J.M., Bahreini, R., Brock, C.A., Holloway, J.S., Lack,
1054 D.A., Middlebrook, A.M., Perring, A.E., Schwarz, J.P., Spackman, J.R., and Nenes, A.: CCN

1055 spectra, hygroscopicity, and droplet activation kinetics of Secondary Organic Aerosol
1056 resulting from the 2010 Deepwater Horizon oil spill, *Environ. Sci. Technol.*, 46, 3093-3100,
1057 2012b.

1058 Moore, R.H., Karydis, V.L., Capps, S.L., Latham, T.L. and Nenes, A.: Droplet Number Prediction
1059 Uncertainties From CCN: An Integrated Assessment Using Observations and a Global Model
1060 Adjoint, *Atmos. Chem. Phys.*, 13, 4235–4251, 2013.

1061 Morales, R., and Nenes, A.: Characteristic updrafts for computing distribution-averaged cloud
1062 droplet number, autoconversion rate effective radius, *J. Geophys. Res.*, 115, D18220,
1063 doi:10.1029/2009JD013233, 2010.

1064 Morales Betancourt, R., and Nenes, A.: Aerosol Activation Parameterization: The population
1065 splitting concept revisited, *Geosci. Mod. Dev.*, 7, 2345–2357, 2014.

1066 Nenes, A. and Seinfeld, J.H.: Parameterization of cloud droplet formation in global climate
1067 models *J. Geophys. Res.*, 108 (D7), 4415, doi: 10.1029/2002JD002911, 2003.

1068 Ng, N. L., Herndon, S. C., Trimborn, A., Canagaratna, M. R., Croteau, P. L., Onasch, T. B.,
1069 Sueper, D., Worsnop, D. R., Zhang, Q., Sun, Y. L., and Jayne, J. T.: An Aerosol Chemical
1070 Speciation Monitor (ACSM) for routine monitoring of the composition and mass
1071 concentration of ambient aerosol., *Aerosol Sci. Tech.*, 45, 780–794, 2011.

1072 Omar, A. H., Winker, D. M., Kittaka, C., Vaughan, M. A., Liu, Z. Y., Hu, Y. X., Trepte, C. R.,
1073 Rogers, R. R., Ferrare, R. A., Lee, K. P., Kuehn, R. E., and Hostetler, C. A.:
1074 The CALIPSO automated aerosol classification and lidar ratio selection algorithm, *J. Atmos.*
1075 *Ocean. Tech.*, 26, 1994–2014, doi:10.1175/2009jtecha1231.1, 2009.

1076 Paramonov M., P. P. Aalto, A. Asmi, N. Prisle, V.-M. Kerminen, M. Kulmala, and T. Petäjä, The
1077 analysis of size-segregated cloud condensation nuclei counter (CCNC) data and its
1078 implications for cloud droplet activation, *Atmos. Chem. Phys.*, 13, 10285–10301,
1079 doi:10.5194/acp-13-10285-2013, 2013.

1080 Petters, M.D., and Kreidenweis, S.M.: A single parameter representation of hygroscopic growth
1081 and cloud condensation nucleus activity, *Atmos. Chem. Phys.*, 7, 1961-1971, doi:
1082 10.5194/acp-8-6273-2008, 2007.

1083 Petters, M.D., Wex, H., Carrico, C.M., Hallbauer, E., Massling, A., McMeeking, G.R., Poulain, L.,
1084 Wu, Z., Kreidenweis, S.M., and Stratmann, F.: Towards closing the gap between hygroscopic
1085 growth and activation for secondary organic aerosol-Part 2: Theoretical approaches, *Atmos.*
1086 *Chem. Phys.*, 9, 3999-4009, 2009.

1087 Pilinis, C., Pandis, S.N., and Seinfeld, J.H.: Sensitivity of direct climate forcing by atmospheric
1088 aerosols to aerosol size and composition, *J. Geophys. Res.*, 100, D9, 18739-18754, 1995.

1089 Prenni, A.J., Petters, M.D., Kreidenweis, S.M., DeMott, P.J., and Ziemann, P.J.: Cloud droplet
1090 activation of secondary organic aerosol, *J. Geophys. Res.*, 112, D10223,
1091 doi:10.1029/2006JD007963, 2007.

1092 Rader, D.J., and McMurry P.H.: Application of the tandem differential mobility analyzer to
1093 studies of droplet growth or evaporation, *J. Aerosol Sci.*, 17, 771-787, 1986.

1094 Remy, S. and Kaiser, J. W.: Daily global fire radiative power fields estimation from one or two
1095 MODIS instruments, *Atmos. Chem. Phys.*, 14, 13377-13390, doi:10.5194/acp-14-13377-
1096 2014, 2014.

1097 Rissler, J., Vestin, A., Swietlicki, E., Fisch, G., Zhou, J., Artaxo, P., and Andreae, M.O.: Size
1098 distribution and hygroscopic properties of aerosol particles from dry-season biomass burning
1099 in Amazonia, *Atmos. Chem. Phys.*, 6, 471-491, 2006.

1100 Roberts, G., Nenes, A., Andreae, M.O., Seinfeld, J.H.: Impact of Biomass Burning on Cloud
1101 Properties in the Amazon Basin, *J. Geophys. Res.*, 108, doi: 10.1029/2001JD000985, 2003.

1102 Roberts, G.C., and Nenes, A.: A continuous-flow streamwise thermal-gradient CCN chamber for
1103 atmospheric measurements, *Aerosol Sci. Technol.*, 39, 206-221,
1104 doi:10.1080/027868290913988, 2005.

1105 Rose, D., Nowak, A., Achtert, P., Wiedensohler, A., Hu, M., Shao, M., Zhang, Y., Andreae, M.
1106 O., Poeschl, U.: Cloud condensation nuclei in polluted air and biomass burning smoke near
1107 the mega-city Guangzhou, China – Part 1: Size-resolved measurements and implications
1108 for the modeling of aerosol particle hygroscopicity and CCN activity, *Atmos. Chem. Phys.*,
1109 10, 3365–3383, doi:10.5194/acp-10-3365-2010, 2010.

1110 Ruehl, C., Chuang, P.Y., Nenes, A., Cappa, C., and Kolesar, K.: New Evidence of Surface
1111 Tension Reduction in Microscopic Aqueous Droplets, *Geoph. Res. Let.*, 39, L23801,
1112 doi:10.1029/2012GL053706, 2012.

1113 Sandradewi, J., Prevot, A. S. H., Szidat, S., Perron, N., Lanz, V. A., Weingartner, E., and
1114 Baltensperger, U.: Using aerosol light absorption measurements for the quantitative
1115 determination of wood burning and traffic emission contributions to particulate matter,
1116 *Environ. Sci. Technol.*, 42, 3316–3323, 2008.

1117 Sciare, J., Bardouki, H., Moulin, C., Mihalopoulos, N.: Aerosol sources and their contribution to
1118 the chemical composition of aerosols in the Eastern Mediterranean Sea during summertime,
1119 *Atmos. Chem. Phys.*, 3, 291–302, doi:10.5194/acp-3-291-2003, 2003.

1120 Sciare, J., Oikonomou, K., Favez, O., Liakakou, E., Markaki, Z., Cachier, H., and Mihalopoulos,
1121 N.: Long-term measurements of carbonaceous aerosols in the Eastern Mediterranean:
1122 evidence of long-range transport of biomass burning, *Atmos. Chem. Phys.*, 8, 5551-5563,
1123 2008.

1124 Seinfeld, J.H., and Pandis, S.N.: *Atmospheric Chemistry and Physics: From Air Pollution to*
1125 *Climate Change*, 2nd edition, J. Wiley, New York, 2006.

1126 Spracklen, D.V., Carslaw, K.S., Pöschl, U., Rap, A., and Forster, P.M.: Global cloud condensation
1127 nuclei influenced by carbonaceous combustion aerosol, *Atmos. Chem. Phys.*, 11, 9067-9087,
1128 doi:10.5194/acp-11-9067-2011, 2011.

1129 Stolzenburg, M.R., and McMurry, P.H.: *TDMAFIT User's Manual*, Particle Technology
1130 Laboratory, Department of Mechanical Engineering, U of Minnesota, Minneapolis, MN 55455,
1131 1988.

1132 Stolzenburg, M.R. and McMurry, P.H.: An ultrafine aerosol Condensation Nucleus Counter,
1133 *Aerosol Sci. Technol.*, 14, 48-65, 1991.

1134 Triantafyllou, E., M. Giamarelou, E. Bossioli, P. Zarmpas, C. Theodosi, C. Matsoukas, M.
1135 Tombrou, N. Mihalopoulos, and G. Biskos: Particulate Pollution Transport Episodes from
1136 Eurasia to a Remote Region of Northeast Mediterranean, *Atmos. Environ.*, 128, 45–52,
1137 doi:10.1016/j.atmosenv.2015.12.054, 2016.

1138 Wiedensohler, A., Birmili, W., Nowak, A., Sonntag, A., Weinhold, K. et al.: Mobility particle size
1139 spectrometers: harmonization of technical standards and data structure to facilitate high
1140 quality long-term observations of atmospheric particle number size distributions, *Atmos.*
1141 *Meas. Tech.*, 5, 657-685, 2012.

1142 Winker, D. M., Vaughan, M. A., Omar, A., Hu, Y., Powell, K. A., Liu, Z., Hunt, W. H., and Young,
1143 S. A.: Overview of the CALIPSO mission and CALIOP data processing algorithms, *J. Atmos.*
1144 *Ocean. Tech.*, 26, 2310–2323, doi:10.1175/2009JTECHA1281.1, 2009.

1145 Wu, Z.J., Poulain, L., Henning, S., Dieckmann, K., Birmili, W., van Pinxteren, D., Spindler, G.,
1146 Müller, K., Stratmann, F., Herrmann, H., and Wiedensohler, A.: Relating particle
1147 hygroscopicity and CCN activity to chemical composition during the HCCT-2010 field
1148 campaign, *Atmos. Chem. Phys.*, 13, 7983-7996, doi:10.5194/acp-13-7983-2013, 2013.

1149 Zamora, L.M., Kahn, R.A., Anderson, B.E., Apel, E., Diskin, G.S., Jimenez, J.L., McFarquhar,
1150 G.M., Nenes, A., Wisthaler, A., Kondo, Y., Zelenyuk-Imre, A., and Ziemba, L.: Aircraft-
1151 measured indirect cloud effects from biomass burning smoke in the Arctic and subarctic,
1152 *Atmos.Chem.Phys.*, 16, 715-738, 2016.

1153
1154

1155 **Table and Figure Captions**

1156 **Table 1:** Calculated chemical dispersion in terms of $\sigma(\kappa)/\kappa$ for the four studied fire
1157 events and all measured particle sizes.

1158

1159 **Table 2:** Average CFSTGC-derived κ_{CCN} values and HTDMA-derived κ_{HTDMA} values for
1160 the selected particles sizes.

1161

1162 **Table 3:** Percentage of externally mixed samples (B_f), the hygroscopic parameter of
1163 the less and more hygroscopic mode (κ_1, κ_2), respectively, and the number fraction
1164 of particles residing in the less hygroscopic mode (N_{f1}) during the Chios event (20-
1165 21/08/2012).

1166

1167 **Table 4:** Same as Table 3, during the Euboea event (03-05/09/2012).

1168

1169 **Table 5:** Variance of N_d and relative contribution to this variance of aerosol number
1170 and chemical composition for the four fire events.

1171

1172 **Figure 1:** Schematic of the setup used for the CCN and mixing state measurements.

1173

1174 **Figure 2:** (a) Satellite composite view from MODIS of the fire plume emerging from
1175 the island of Chios on 18 August 2012 (courtesy on NASA). The blue and red lines
1176 delineate the two ground tracks of the CALIPSO satellite during its overpass over Crete
1177 on 19 August 2012 between 00:27-00:40 and 11:34-11:47 UTC, (b) Vertical profiles
1178 of the aerosol backscatter coefficient (in $\text{km}^{-1}\text{sr}^{-1}$) at 532 and 1064 nm (left) and linear
1179 particle depolarization ratio at 532 nm (right) measured by CALIPSO and (c) Vertical
1180 profiles of the aerosol subtypes captured by CALIPSO during its overpass over Crete;
1181 the marked area is located at the NW of Finokalia station (00:27-00:40 UTC).

1182

1183 **Figure 3:** Time series concentrations of major PM_{10} species that contribute in the
1184 identification of the BB events. The shaded areas represent the four considered fire
1185 events.

1186

1187 **Figure 4:** CCN concentrations for the selected particle sizes during the arrival of the
1188 smoke plumes for (a) Chios, (b) Croatia, (c) Euboea and (d) Andros. The black solid
1189 line represents the biomass burning component of the organic aerosol at the given
1190 time.

1191

1192 **Figure 5:** Activation fractions for the selected particle sizes during the arrival of the
1193 smoke plumes for (a) Chios, (b) Croatia, (c) Euboea and (d) Andros. The brown solid
1194 line represents the processed biomass burning component of the organic aerosol.

1195

1196 **Figure 6:** Characteristic hygroscopicity parameters of the selected particle sizes for
1197 (a) Chios, (b) Croatia, (c) Euboea and (d) Andros. The solid line represents the biomass
1198 burning component of the organic aerosol at the given time and the shaded areas
1199 represent the smoke plume influence period.

1200

1201 **Figure 7:** Hygroscopicity parameters derived from the HTDMA (a) & (c) and number
1202 size distributions from the SMPS (b) & (d) for the Chios and Euboea fire events,
1203 respectively. The shaded areas represent the smoke plume influence period.

1204

1205 **Figure 8:** Average diurnal contribution of each organic aerosol factor to the κ_{org}
1206 computed by multiplying the mass fraction by the corresponding inferred
1207 hygroscopicity parameter and the predicted diurnal profile of the total κ_{org} in the
1208 ambient aerosol.

1209

1210 **Figure 9:** Maximum supersaturation (S_{max}) (left panels) and potential droplet number
1211 (N_d) (right panels) for the four fire events of Chios (a,b), Croatia (c,d), Euboea (e,f)
1212 and Andros (g,h).

1213

1214 **Figure 10:** Droplet number concentration (top panel) and cloud maximum
1215 supersaturation (bottom panel) for each fire event as a function of BB influence,
1216 expressed by the sum of BBOA and OOA-BB ACSM factors.

1217

1218 **Table 1**

	<i>60 nm</i>	<i>80 nm</i>	<i>100 nm</i>	<i>120 nm</i>
<i>Chios</i>	0.85±0.14	0.73±0.14	0.60±0.20	0.41±0.16
<i>Croatia</i>	0.77±0.18	0.68±0.19	0.44±0.12	0.41±0.10
<i>Euboea</i>	0.70±0.20	0.49±0.10	0.32±0.08	0.29±0.06
<i>Andros</i>	0.71±0.10	0.52±0.13	0.34±0.10	0.30±0.06

1219

1220

1221 **Table 2**

	K_{HTDMA}	K_{CCN}
<i>60 nm</i>	0.23±0.07	0.22±0.05
<i>80 nm</i>	0.28±0.10	0.39±0.10
<i>100 nm</i>	0.30±0.10	0.44±0.10
<i>120 nm</i>	0.33±0.11	0.49±0.13

1222

1223

1224 **Table 3**

d_p (nm)	Bf (%)	κ_1	Nf_1	κ_2
60	6.90	0.05±0.02	0.17±0.06	0.18±0.01
80	20.0	0.05±0.02	0.33±0.14	0.19±0.03
100	23.0	0.06±0.03	0.43±0.24	0.21±0.04
120	30.4	0.05±0.03	0.47±0.19	0.20±0.04

1225

1226

1227 **Table 4**

d_p (nm)	Bf (%)	κ_1	Nf_1	κ_2
60	5.30	0.09±0.07	0.37±0.34	0.31±0.19
80	15.2	0.06±0.04	0.31±0.17	0.20±0.03
100	26.5	0.05±0.03	0.39±0.19	0.19±0.03
120	28.2	0.05±0.03	0.40±0.19	0.19±0.03

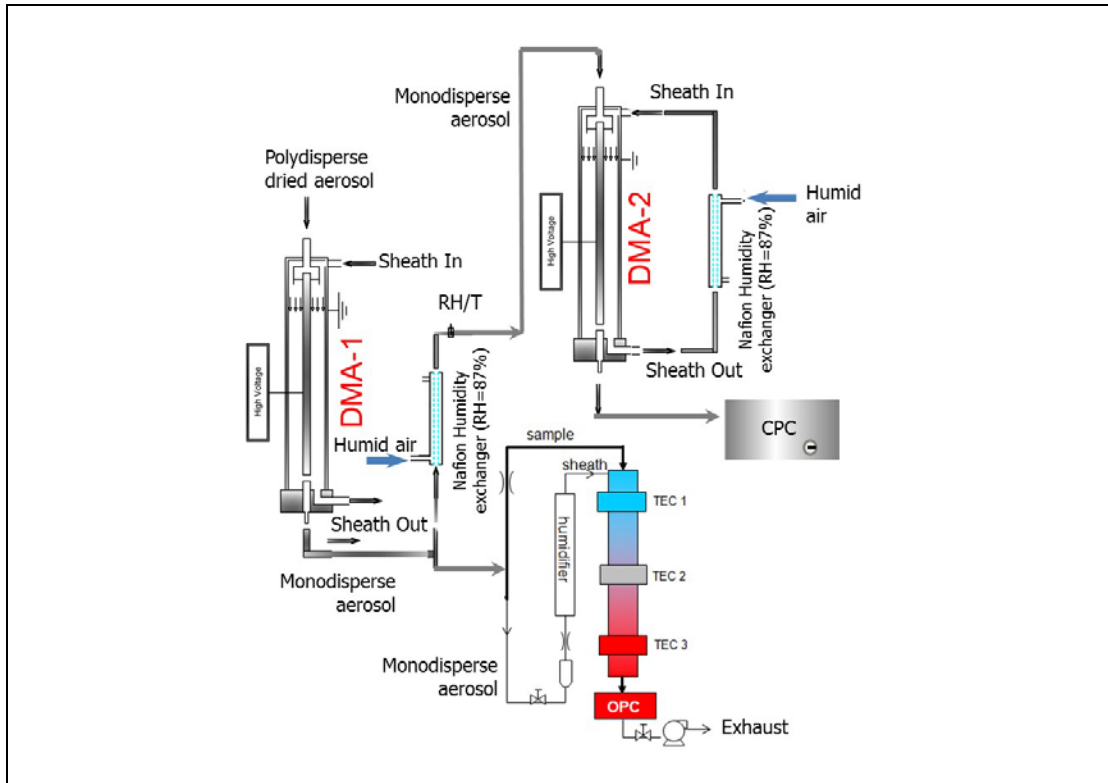
1228

1229 **Table 5**

	$Variance_{Na}$		$Contribution_{\kappa}$		$Contribution_{N_{aerosol}}$	
	$w=0.3$	$w=0.6$	$w=0.3$	$w=0.6$	$w=0.3$	$w=0.6$
<i>Chios</i>	13.8	18.1	17.7%	12.6%	82.3%	87.4%
<i>Croatia</i>	34.4	47.7	26.7%	25.2%	73.3%	74.8%
<i>Euboea</i>	60.9	111.3	1.10%	2.2%	98.9%	97.8%
<i>Andros</i>	164.2	307.8	0.10%	0.15%	99.9%	99.8%

1230

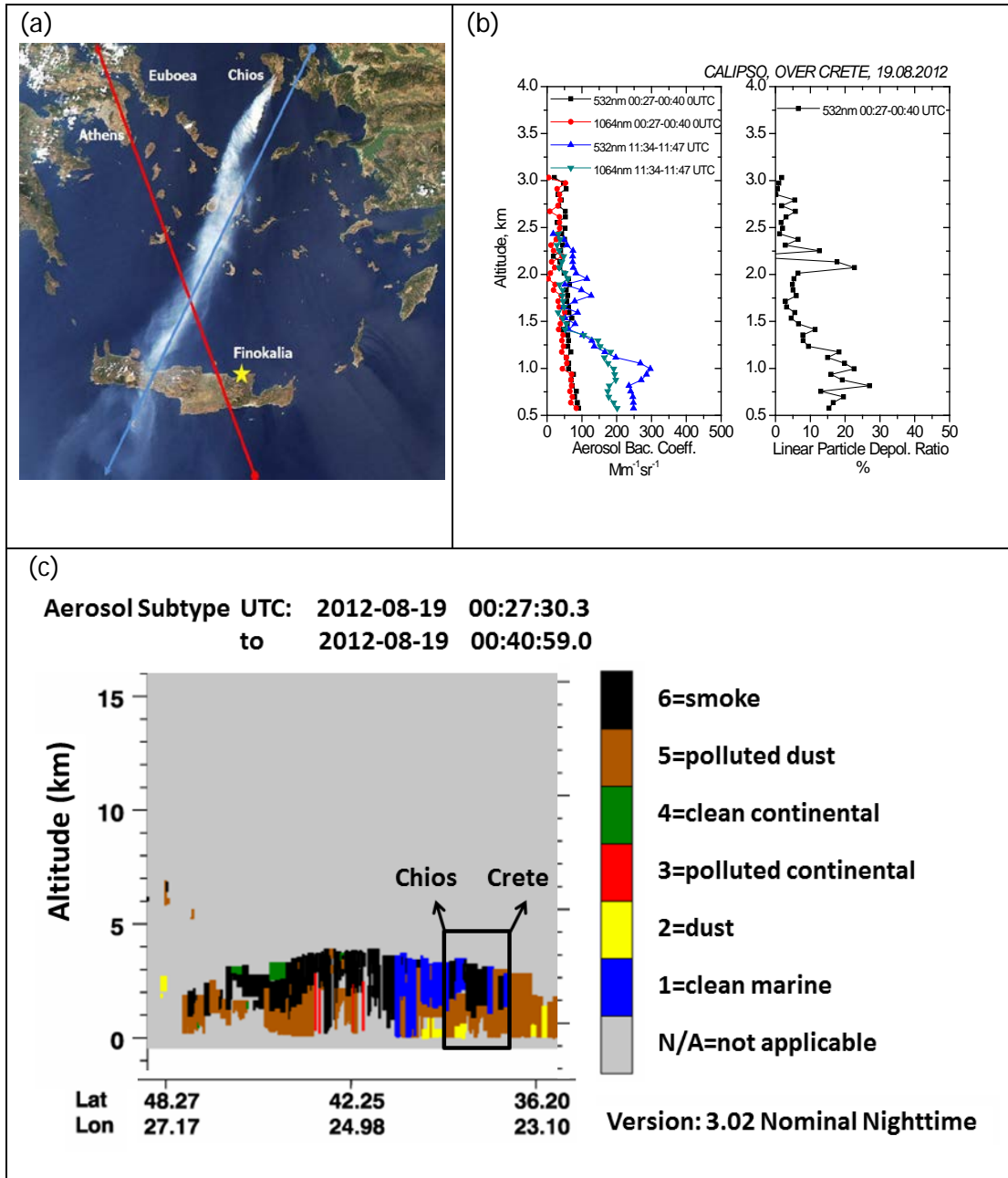
1231 **Figure 1**



1232

1233

Figure 2

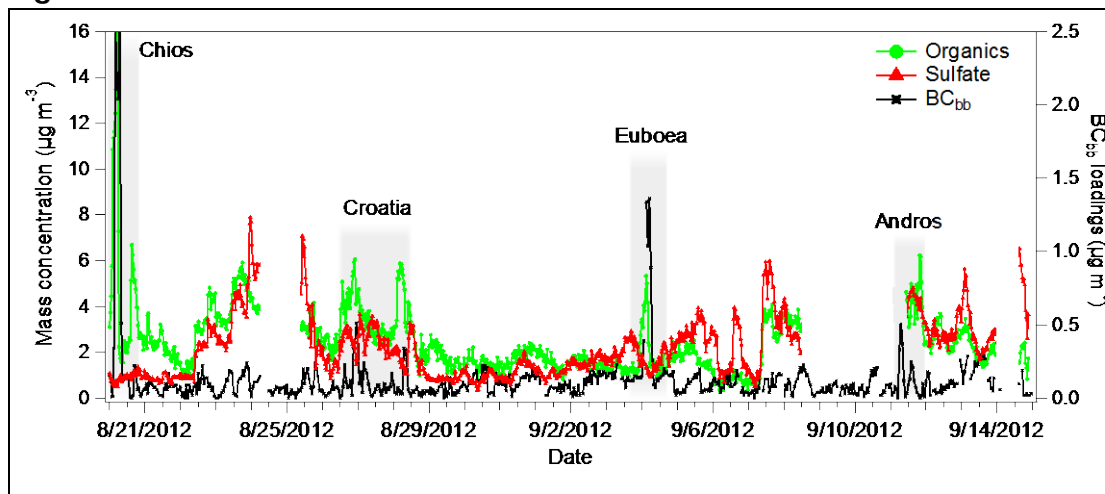


1234

1235

1236

Figure 3

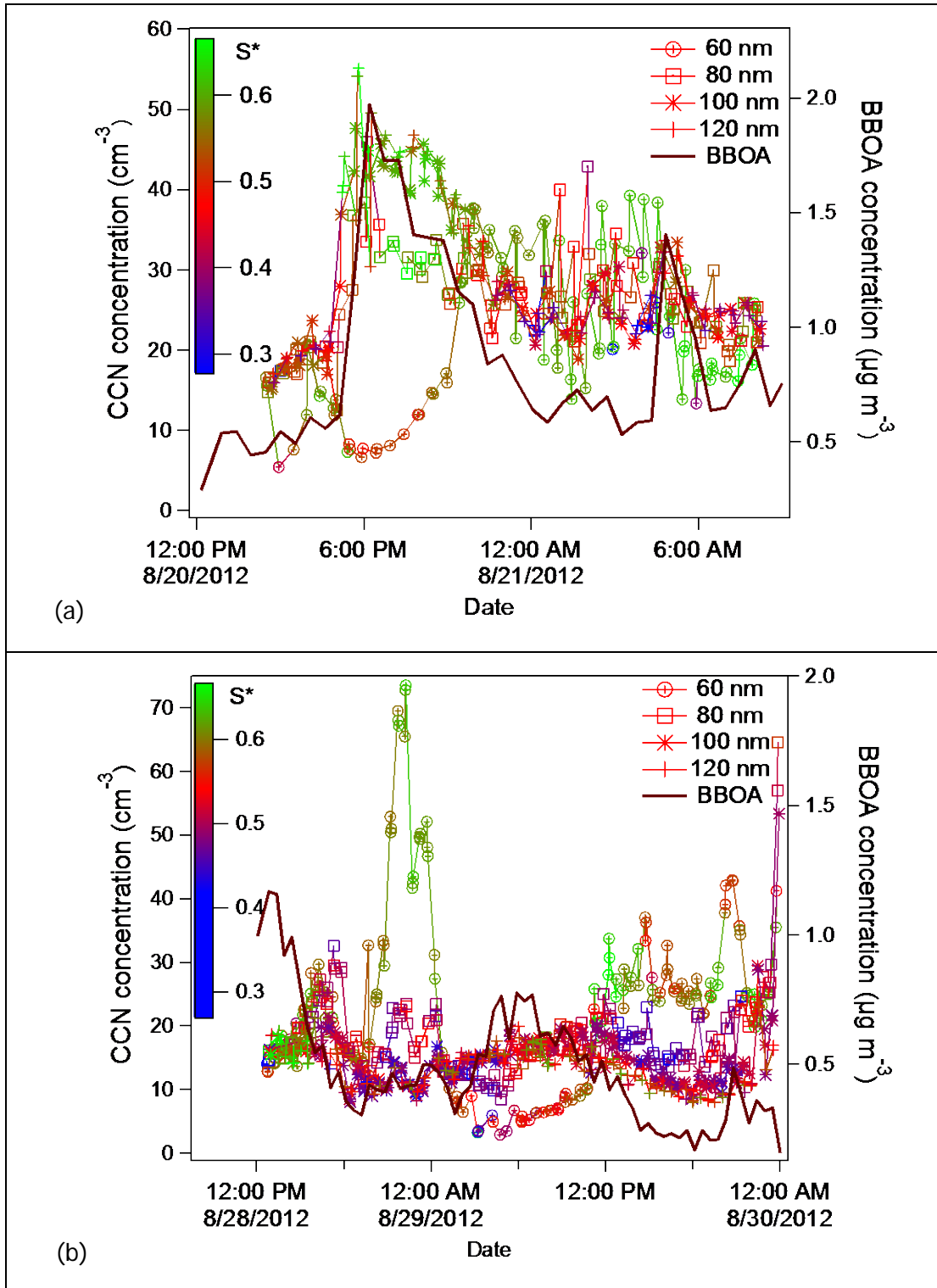


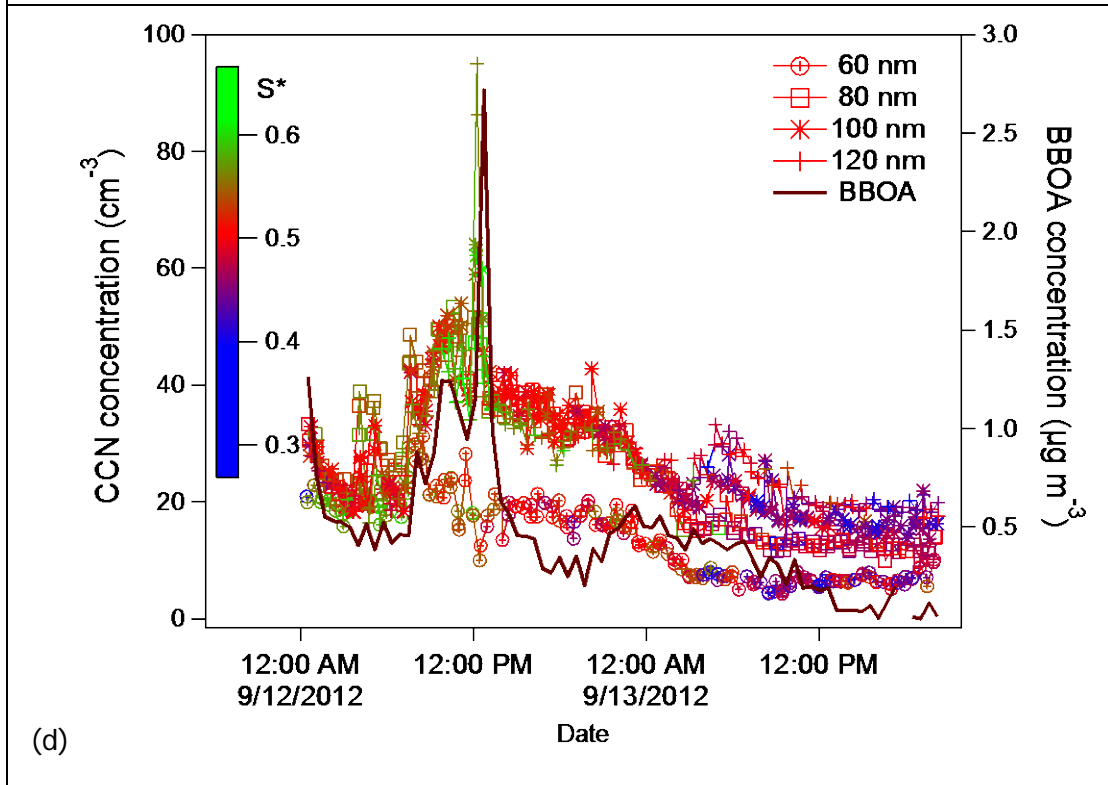
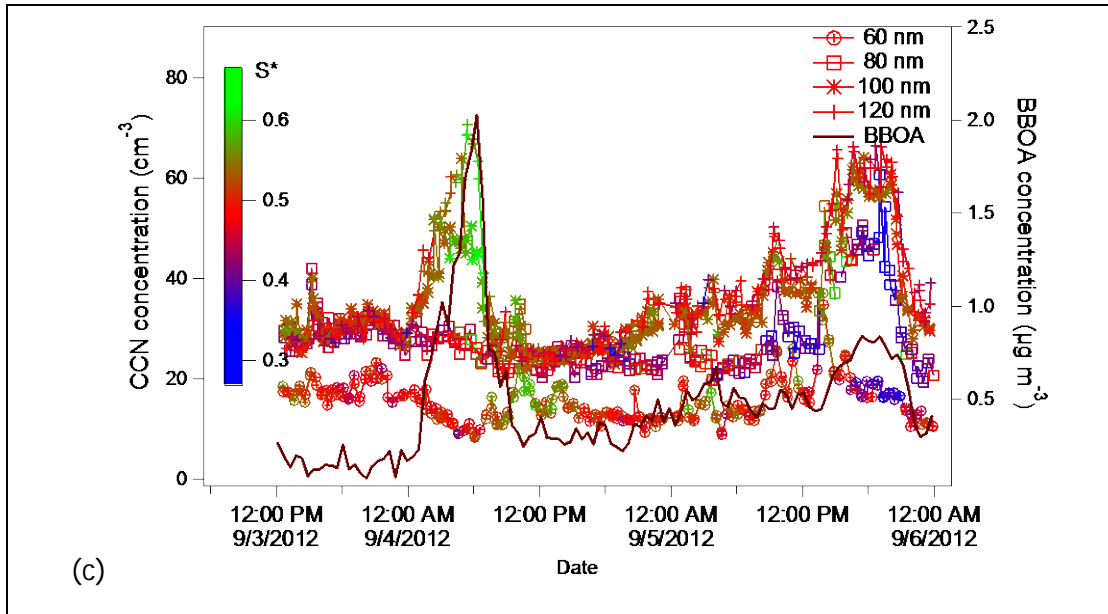
1237

1238

1239

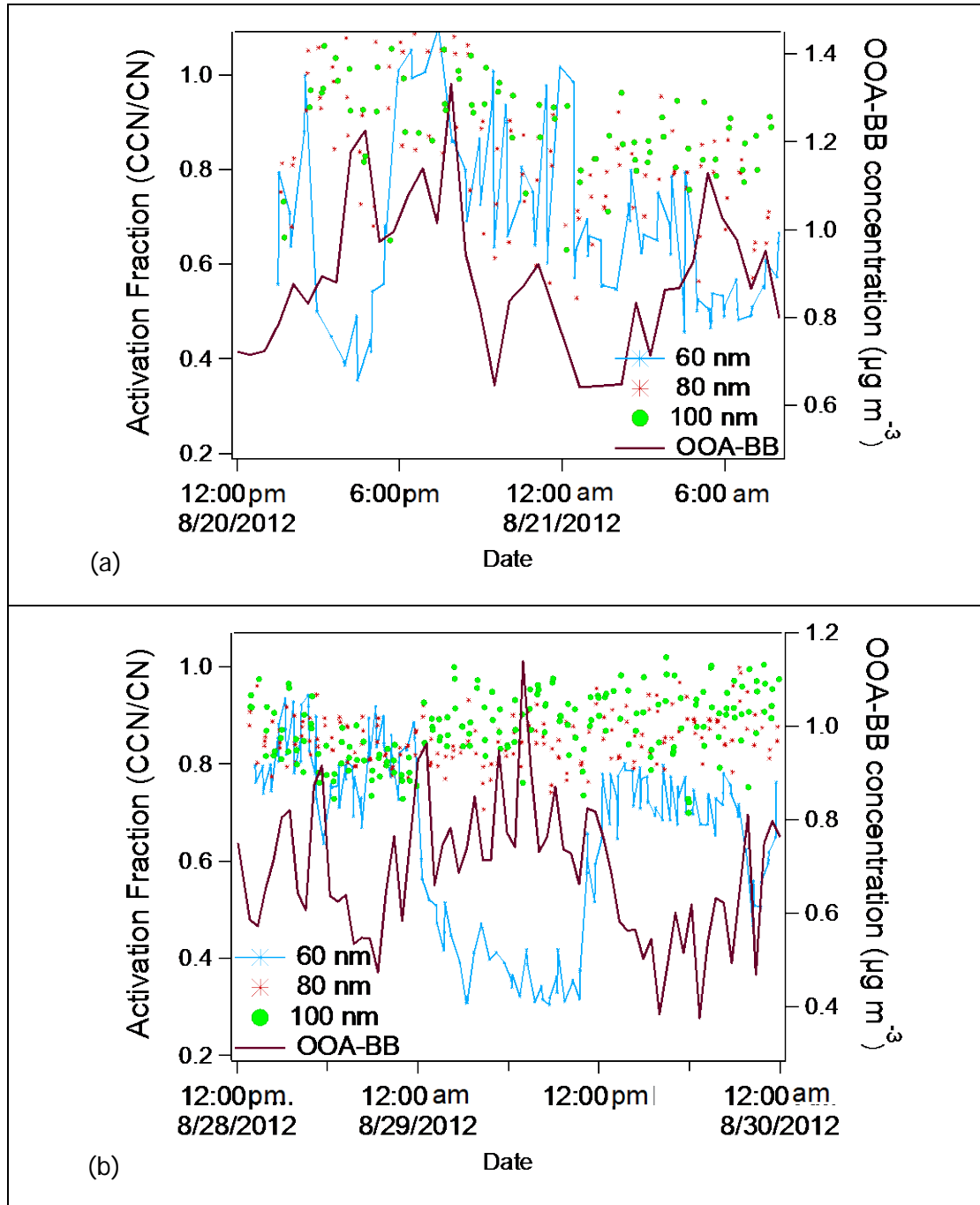
Figure 4

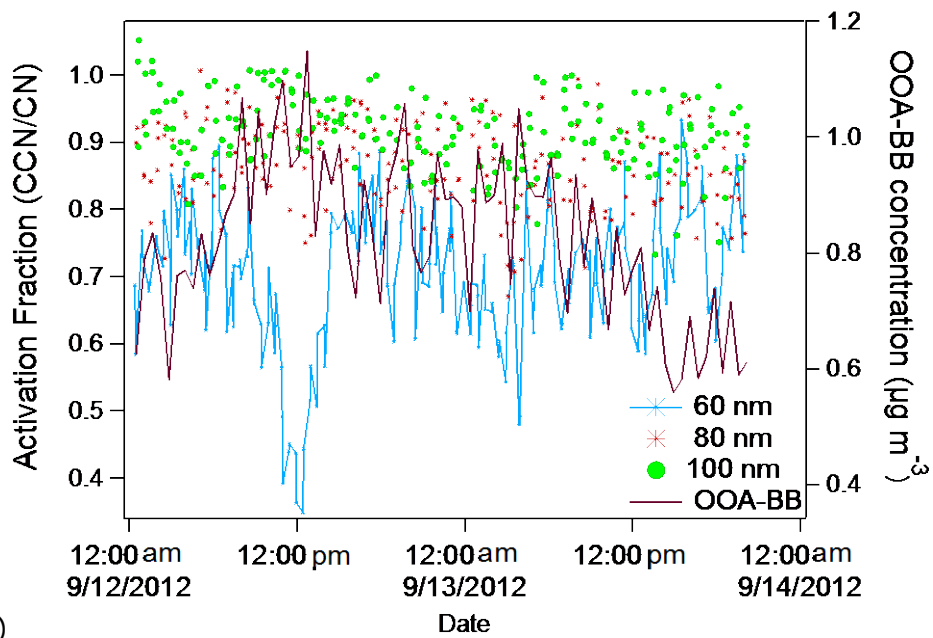
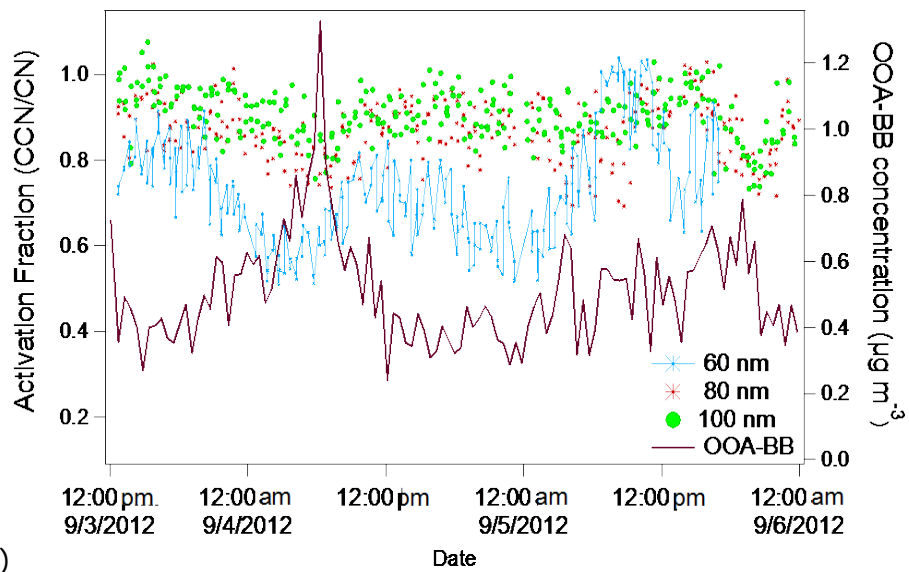




1241
1242

Figure 5

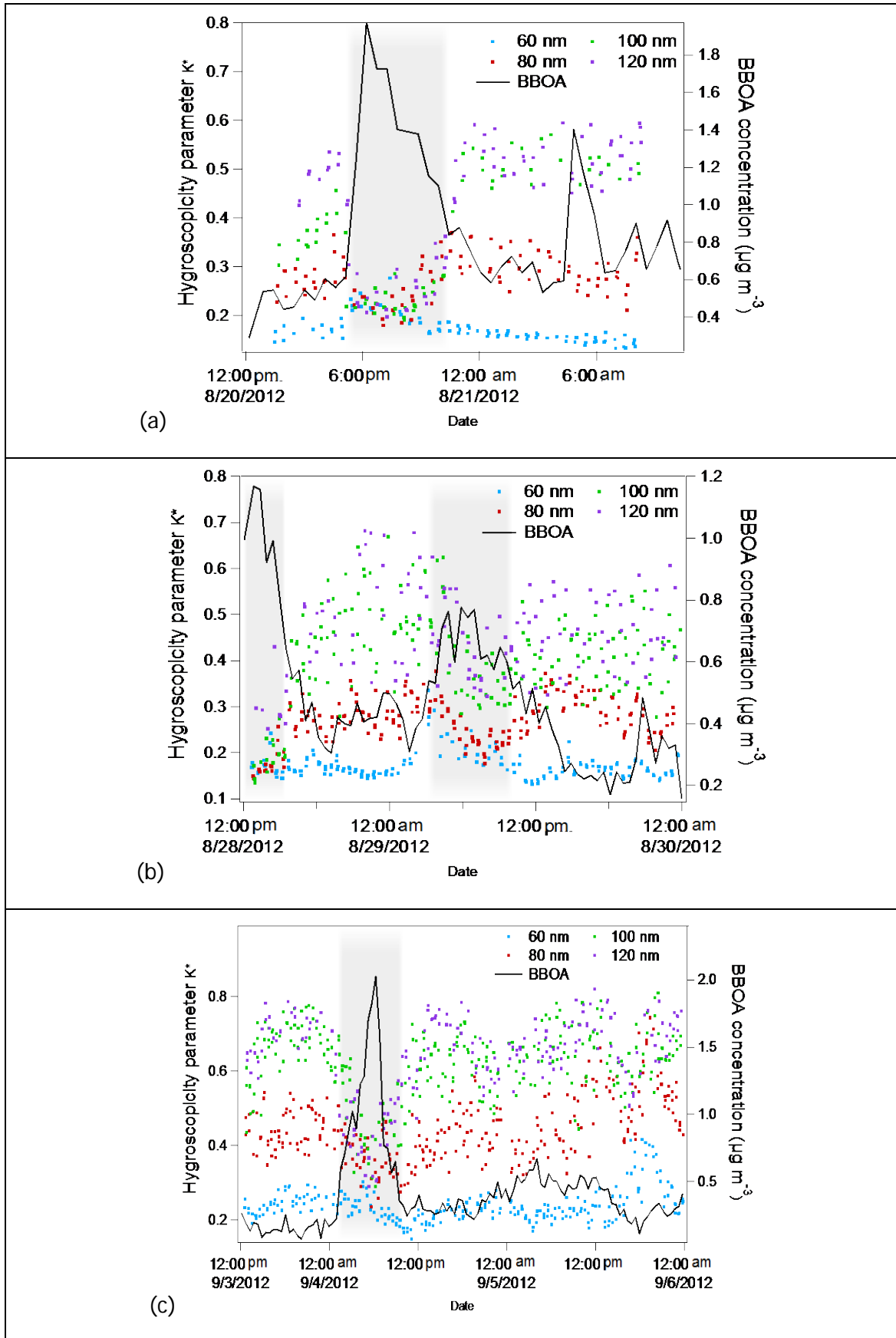


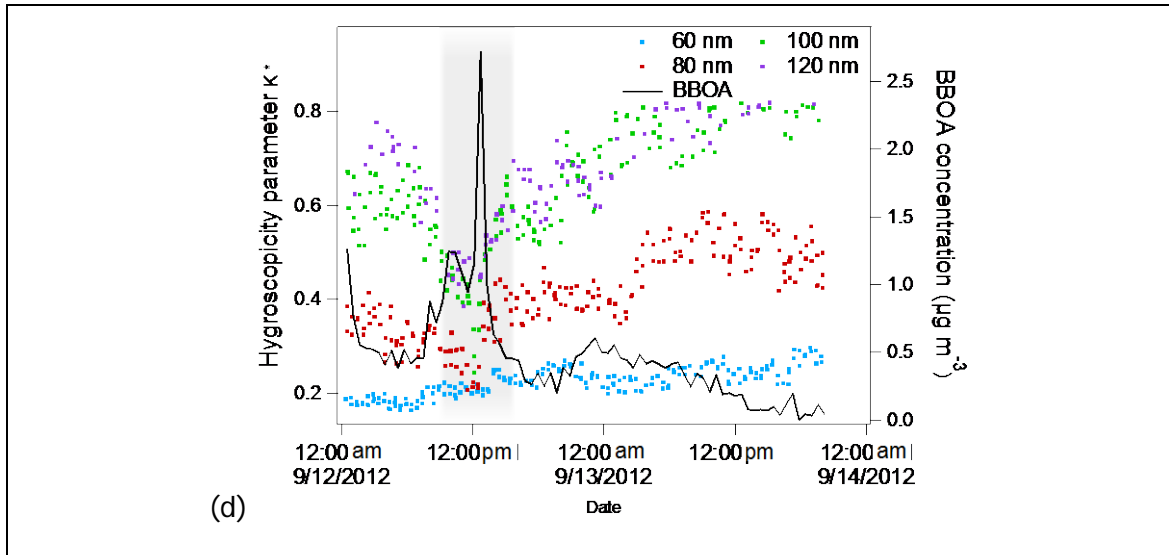


1244

1245

Figure 6

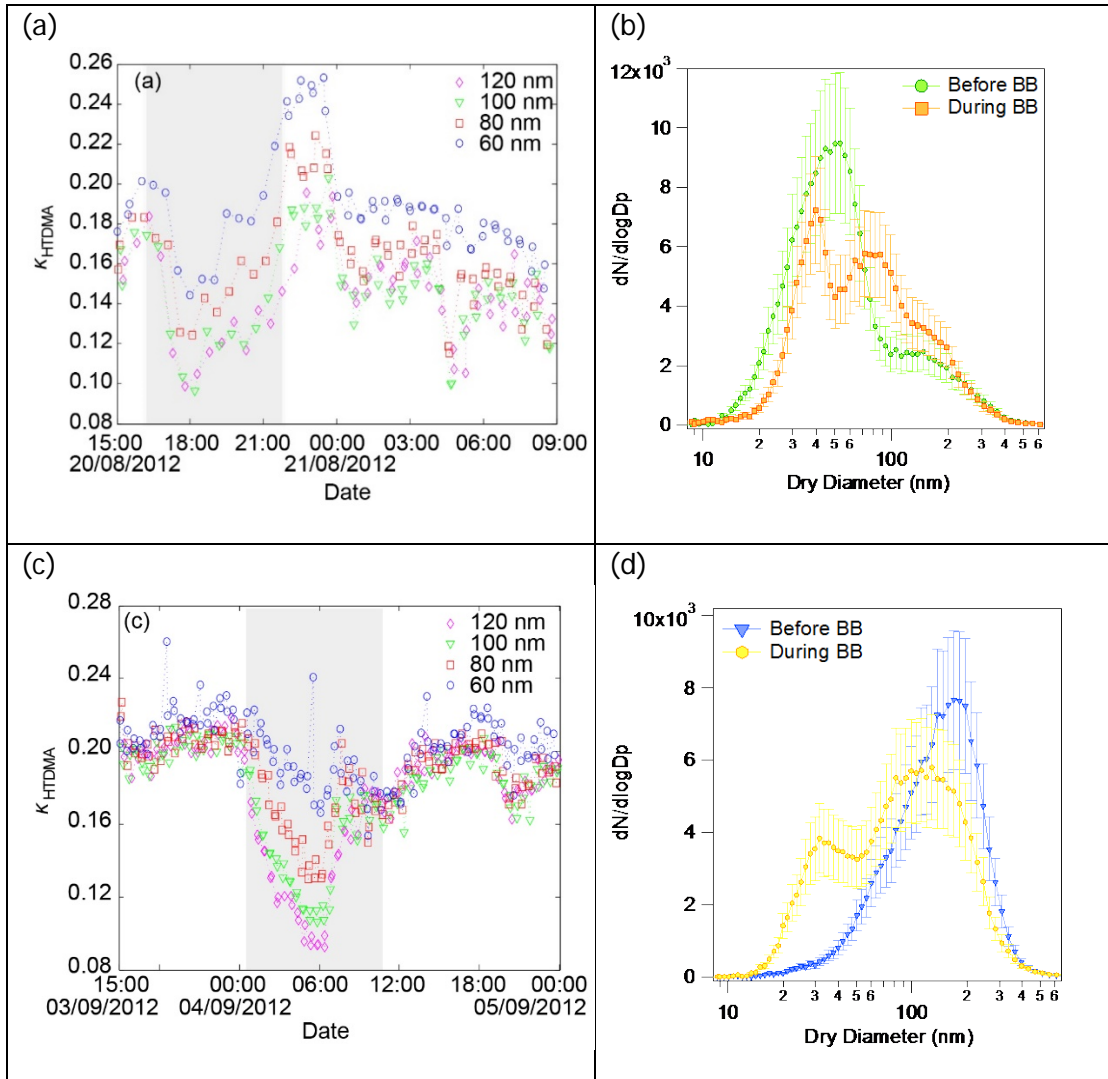




1247
1248

1249

Figure 7

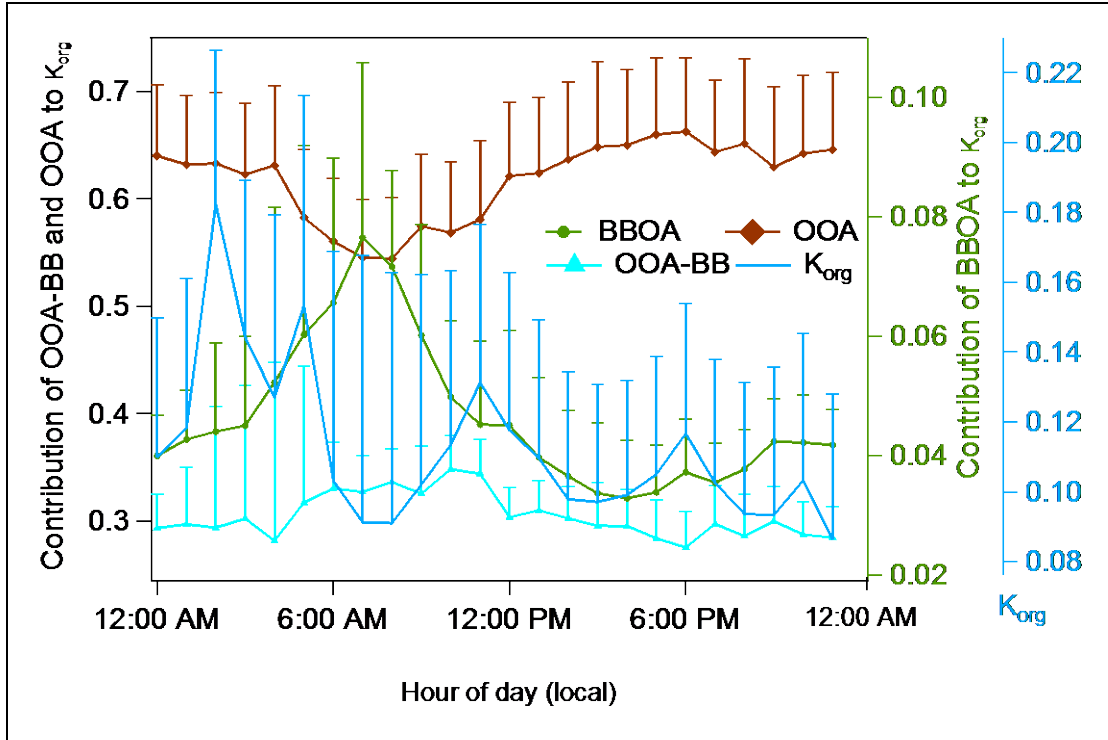


1250

1251

1252

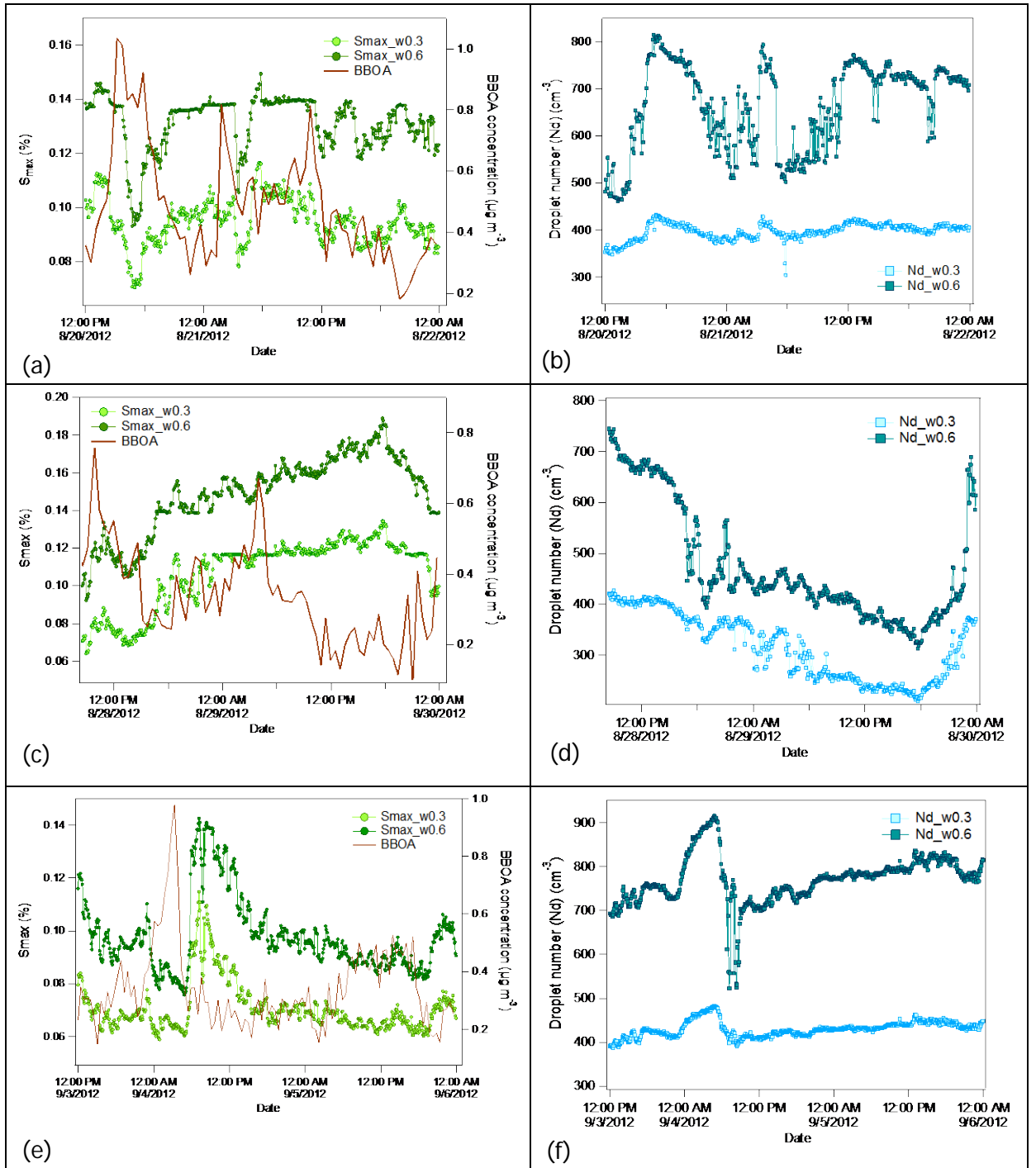
Figure 8

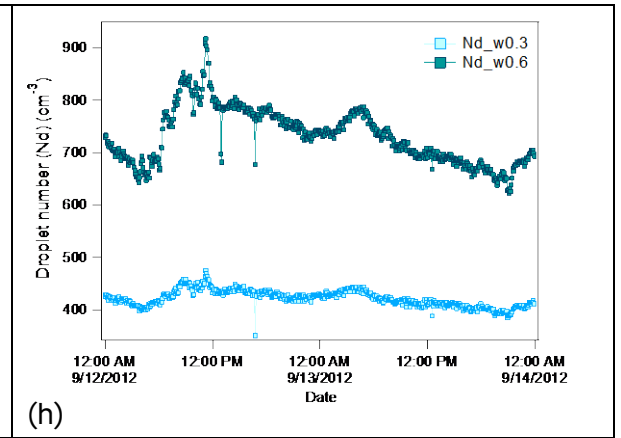
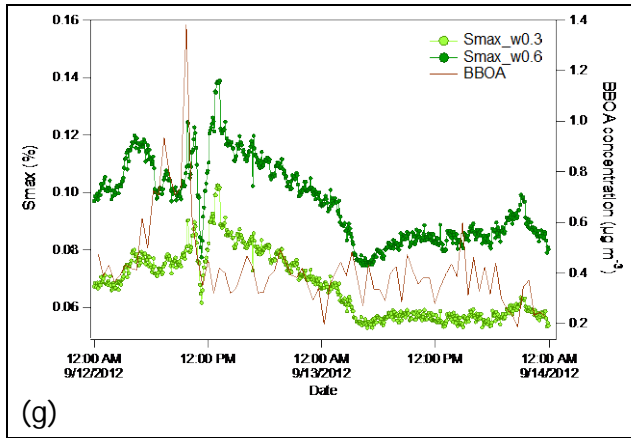


1253

1254

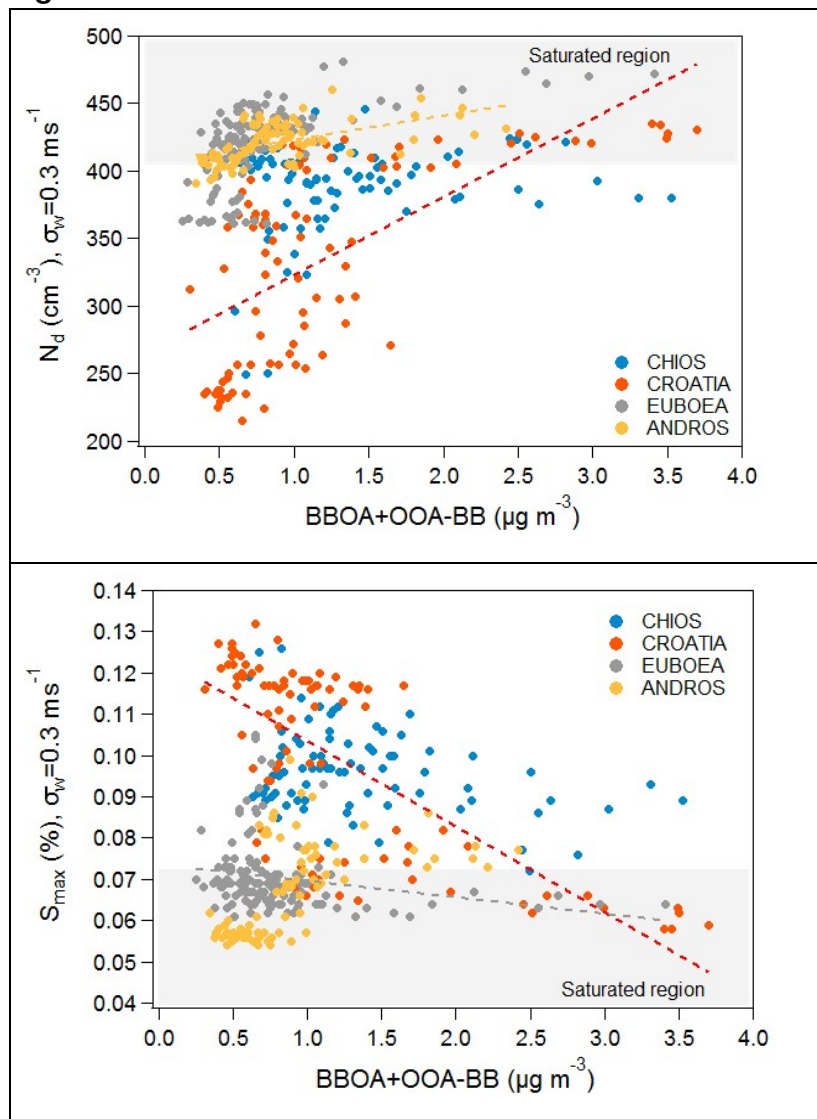
Figure 9





1256
1257

1258 **Figure 10**



1259

1260

1261